EMI Mitigation of a Ćuk-Based Power-Electronic System Using Switching-Sequence-Based Control

Debanjan Chatterjee, *Student Member, IEEE*, and Sudip K. Mazumder, *Fellow, IEEE*

***Abstract*—Switching-sequence-based control (SBC) laws when designed based on topological switching behavior can have positive effects on slow- and fast-scale dynamics of a power-electronic system (PES). The slow-scale control can encompass fast PES state regulation and tracking, based on predefined objective, while fast-scale control can address differential-mode (DM) and common-mode (CM) spectral-peak energy associated with PES switching operation. Such control laws may offer enhanced programmability to conventional PES design where bulky electromagnetic interference (EMI) filters have been traditionally used to reduce EMI of switching power converters to meet EMI regulatory standards. An EMI filter is always a less programmable solution since it is usually designed for the worst-case EMI mitigation and usually overkill for a PES operating under reduced load condition. The control scheme outlined in this article offers EMI mitigation across wide operating regions without compromising PES regulation. Moreover, it does so by use of switching sequences that guarantee the reachability of the PES dynamics using an advanced Lyapunov-function-based approach. SBC is a powerful tool to generate control actions for a PES based on multivariate PES state constraints. Hence, contemporary EMI regulatory standards are used as constraints in the SBC formulation to operate the PES under wide operating regime while autonomously mitigating the EMI levels. The work may be of paramount importance for operating the ultra-fast-transition recent wide-bandgap semiconductor devices like GaN–FET and SiC MOSFET under higher power with increasing switching frequencies, which is usually desirable for increased power density and reduced switching losses. Here, a hardware Ćuk–PES operated with GaN–FETs is fabricated and is used for case illustration. It is shown by experimental results how SBC mitigate DM and CM EMI noise of the PES while maintaining regulation even for the higher order nonminimum phase PES, while reducing sensor requirements using state observer derived from the switching model of the PES.**

***Index Terms*—Common-mode (CM) noise, control, differential-mode (DM) noise, electromagnetic interference (EMI), GaN–FET, Lyapunov, switching-sequence-based control (SBC).**

Manuscript received August 19, 2020; revised October 22, 2020 and December 28, 2020; accepted February 9, 2021. Date of publication February 17, 2021; date of current version June 1, 2021. This work was supported in part by the U.S. Office of Naval Research No. N00014-17-1-2695 and in part by the U.S. Department of Energy's Office of Energy Efficiency and Renewable Energy under Solar Energy Technologies Office Agreement No. EE0008349. Recommended for publication by Associate Editor F. Luo. *(Corresponding author: Sudip K. Mazumder.)*

The authors are with the Department of Electrical and Computer Engineering, University of Illinois at Chicago, Chicago, IL 60607-7101 USA (e-mail: dchatt4@uic.edu; mazumder@uic.edu).

Color versions of one or more of the figures in this article are available online at https://doi.org/10.1109/TPEL.2021.3059906.

Digital Object Identifier 10.1109/TPEL.2021.3059906

I. Introduction

RAPID switching transition of wide-bandgap semiconductor devices like GaN, SiC MOSFET, JFET cascodes, etc. have made higher switching frequencies realizable at higher power [1], [2]. This is because, for hard-switched topologies, very-fast edge transitions of the PES switches lead to lower switching losses. This helps in the synthesis of a power-dense/compact power-electronic system (PES). However, rapid switching at increasingly higher frequencies negatively affects electromagnetic interference (EMI) performance of a PES. Hence, EMI input filters need to be designed to fulfil the strict EMI regulatory standards [3] on differential-mode (DM), common-mode (CM), and radiative noise spectrum. The situation can be explained by the following case illustration for conducted noise (CM and DM): operating one of the GaN–FET-based PES modules in [1] at 500 W for rated input and output voltages and a switching frequency of 200 kHz, will result in the violation of the less strict CISPR/EN 55022/32 Class A EMI limit by a margin high enough to necessitate EMI filter that increases space and specific weight of a PES [4], [5]. Use of multistage EMI filters [6] may preclude the use of higher value passive components, thereby reducing EMI filter size and boosting the power density of the PES. Notwithstanding, this causes a predicament in the design of a PES that has relatively low stability margins in closed loop, since the EMI filter may incorporate additional phase lag which may lead to instability and degraded PES overall control performance [7]. This adversely affects the power density of the PES that is supposed to increase with the use of fast switching transition GaN–FETs operating at very high frequencies. It also negatively impacts the efficiency of the PES due to extra losses incurred in the EMI filters [7]–[9].

Due to the stringent limits on the size of the CM capacitor based on the leakage current allowance of the PES [10]–[13], CM EMI filter adversely affects the size of a PES more than DM filter. In DM filter, the size of the DM capacitor can be increased to keep the inductor size down for high-current applications. But CM filter precludes this flexibility [10]–[13], which results in high inductance values for CM EMI cut-off.

To address the issues related to EMI filter design as portrayed in Fig. 1, control-hardware integrated solutions must be woven fine for GaN–FET-based wide bandgap (WBG) PES to realize higher frequency (HF) operation at increased power levels. This is because reliance on an increased size of EMI filters alone will impede the HF operation of a WBG PES.

Frequency modulation techniques with open-loop control have been studied previously to decrease the EMI levels of a PES.

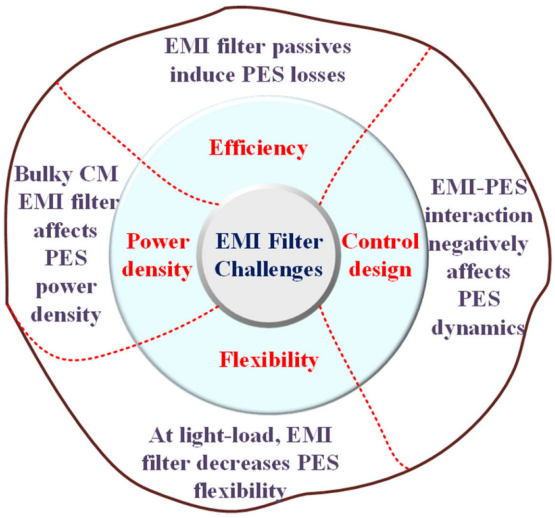

Fig. 1. Illustration of the shortcomings of the traditional EMI filter.

The theory is based on [14] which derives the differential equations to show how frequency modulation impacts the spectrum of a signal. The effectiveness of such methods in terms of EMI reduction of PES for different modulation profiles is discussed in [15]–[17]. Lorenzo [16] focuses its discussion on how to create modulation profiles, with extensive analysis, to have a positive effect on both CM and DM EMI of a PES, while Lin and Chen [18] provide a generalized assessment of how the depth and breadth of the modulation profiles impact PES EMI. They also talk about the significant generalized side effects, such as audible noise due to frequency variation, and poor converter output voltage regulation obtained due to the modulation techniques. However, most of the abovementioned literature determines the effect of the modulating techniques based on open-loop principle only. The literature preferred nonvariation of the PES duty cycles, in order not to disturb the observability of the desired modulation effect on the PES. Also, the modulation techniques do not take into consideration the stability of the PES for change in operating conditions. Moreover, the impact of the modulation on PES behavior on EMI filter design and output filter size has not been discussed. Santolaria [19] outlines the benefits of the open-loop frequency modulation techniques against the drawbacks in increased output voltage ripple but it does not provide any quantitative analysis on how much the output filter size needs to be altered to support constant output voltage against decreased EMI filter size across wide switching frequency range. Moreover, it mainly comments on the open-loop behavior only with predefined constant time allocated switching sequences (SSs). Stepins [20] further highlights the deterioration of the PES state response due to the low-frequency perturbation introduced by frequency modulation under the closed-loop linear controller but precludes detailed analysis on the controller tuning parameters for the experimental responses. Hence, contrary to prevalent literature, the aim is to design a closed-loop controller that yields SSs: 1) which ensures that the PES satisfies the EMI standards [3], 2) reachability of PES dynamics is ensured, and 3) minimize low-frequency output voltage oscillations that may result from 1.

Practically, a PES may be required to operate most of the times in closed-loop under wide operating ranges. Hence, it is necessary to undertake studies related to PES behavior in closed-loop under the influence of EMI mitigating SSs. SSs affect the PES switching behavior, which in turn influences the EMI signature of a PES. They can be synthesized by a model-/data-driven intelligent controller to positively affect the PES EMI signature, which can reduce the EMI size requirements or preclude the need for EMI filters up to some desired power levels.

The SSs can be synthesized based on model predictive control (MPC) theory [21]–[28]. MPC solves multiobjective optimal-control problems by careful manipulation of the switching states of a PES by minimizing a predefined cost function. The work in [21]–[28] solve such problems for a variety of converters that yield better transient response to load variations along with better PES performance metrics. Over and above, [25] shows how optimal controllers can control the switching states of a PES to achieve objectives ranging from limited switching loss reduction to the shaping of PES low-frequency spectrum along with standard PES state regulation. Although MPC uses a mathematical model of the PES to make future predictions, the methods employed and discussed in [21]–[28] makes realization possible to be achieved in real time in current industrial processors for power electronics.

Switching-sequence-based control (SBC) goes a step further to formulate an advanced MPC that controls fast- and slow-scale PES objectives but with SSs that are stability bounded [29]–[31]. Fig. 2(a) shows how SBC is distinct from conventional MPC. SBC uses offline stability/reachability analysis on the feasible SSs of a PES [31] to yield reachable SSs, which ensure PES stability in real time and under challenging loading conditions and saving online computation time [30]. The reachable SSs help to solve an online optimization problem to come up with direct control actions and preclude the need for a modulator. Also, SBC uses piecewise discrete maps of a PES since they can be written easily for digital processors and can increase control bandwidth [30]. Switching state is controlled in a planning horizon in MPC, while the SS evolves; SBC in contrast, directly controls the stability-bound SS.

SBC design is delineated in [29], [30] with adequate case illustrations, where SBC is used to control challenging naval pulsating loads, as well as HF-link inverters leading to enhanced system performance. However, [29], [30] do not address issues related to PES EMI and hence the present work differs from past work on SBC in terms of control formulation, algorithm, and real-time implementation.

This article uses constraints of EMI standards in the SBC formulation to yield PES EMI levels at an acceptable level. Fig. 2(b) illustrates the difference between this article and [29], [30]. The SBC performs EMI mitigation of a PES while maintaining PES output voltage regulation. Although a dc/dc Ćuk converter has been used as a case illustration for the SBC control scheme, the control can encompass other dc/dc applications ranging from road vehicle electric propulsion, adapters, smart lighting

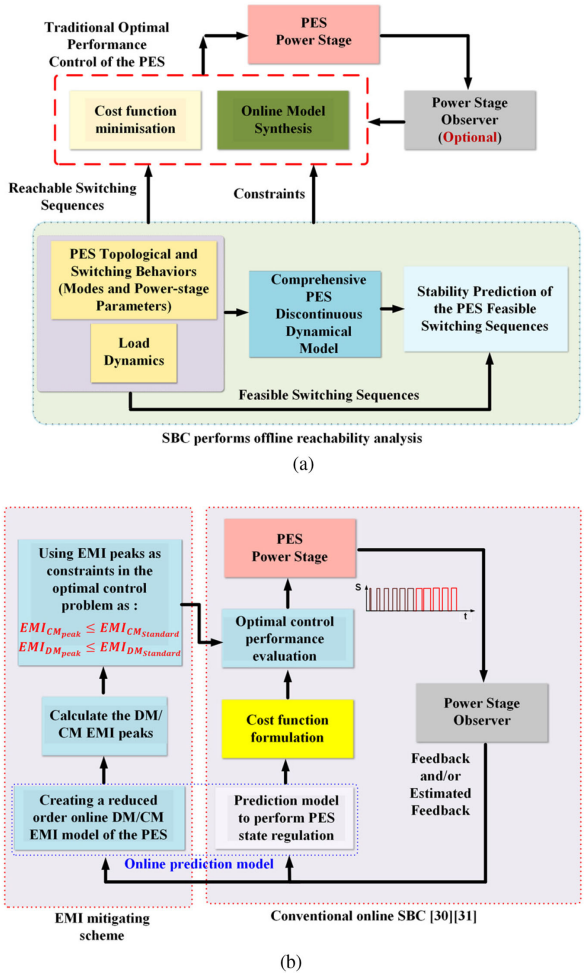

Fig. 2. (a) Distinction between conventional optimal control/MPC and SBC. (b) Conventional SBC [29], [30] modified by to mitigate PES EMI.

applications, etc. For the PES under study (i.e., Ćuk converter), the peaks of a DM and CM model have been used as constraints in the SBC formulation to eliminate the DM filter and reduce the size of the CM filter. This is because a DM EMI model (compared to a CM EMI model) is relatively easier to formulate given its reduced dependency on circuit parasitic.

The article is subdivided as follows. Section II outlines the discrete modeling of the PES and creates an optimal SBC framework for EMI mitigation. Section III delineates a case illustration of the method for a Ćuk–PES. The results are discussed in Section IV, which shows the autonomous EMI reduction under wide operating conditions using SBC and its effects on DM and CM filter size reductions. In Section V, the conclusion is drawn on the efficacy of the SBC for EMI mitigation. The Appendices contain necessary mathematical derivations, and some important nomenclature to help comprehension.

II. SBC Synthesis for EMI Mitigation

Fig. 3(a) and (b) illustrates two different SSs applied to a dc/dc PES yielding the same voltage regulation for a given input voltage. The first SS has a constant time horizon of T_{kw_s}, while the second SS has a variable time horizon given

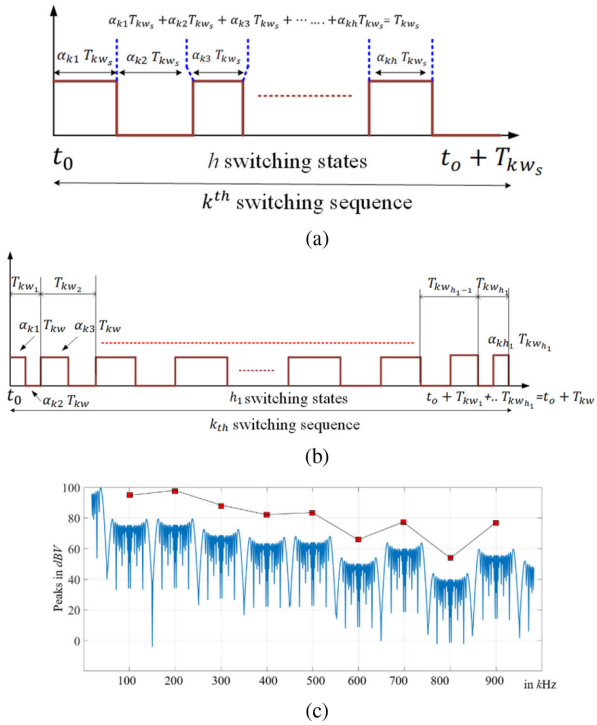

Fig. 3. (a) and (b) Illustrations of two different SSs having different time horizons leading to (c) different EMI levels when applied to the same PES.

by $T_{\mathrm{kw}} = (T_{\mathrm{kw}_1} + \cdots + T_{\mathrm{kw}_s} + \cdots + T_{\mathrm{kw}_{h_1}})$, where $T^{-1}_{\mathrm{kw}_i} = T^{-1}_{\mathrm{kw}_s} + \Delta T^{-1}_{\mathrm{kw}} \mathrm{v}_m(w_m t) \; \forall \; i \in \{1, n\}$, $\Delta T_{\mathrm{kw}} = kT_{\mathrm{kw}_s}$, $k \in R$, and v_m is a periodically varying function with w_m as its angular frequency. The symbols $\alpha_{k1}, \ldots, \alpha_{kh}$ in Fig. 3 denote the time allocation of the switching states [h switching states in Fig. 3(a) and h_1 switching states in Fig. 3(b)] in the SS. Fig. 3(c) illustrates the difference in the conducted-EMI spectrum of the PES in steady state subjected to these two SSs. We observe that, by modulating the T_{kw} of the SS for case illustrated in Fig. 3(b) instead of repeating the same T_{kw} ($= T_{\mathrm{kw}_s}$) for the case illustrated in Fig. 3(a) yields EMI peak reduction as illustrated in Fig. 3(c).

While the control of an SS modulates the fast EMI-scale dynamics, it may also affect slower scale PES dynamics that impact state regulation. Hence, an SBC formulation that controls the fast- and slow-scale dynamics of a PES yielding conducted-EMI mitigation and voltage regulation is synthesized and outlined in the following subsections.

A. PES Modeling and Stability Analysis

In SBC, in contrast to MPC, first, it is ensured, using comprehensive offline computations incorporating PES model and load dynamics, whether a given feasible SS (determined for a PES following [31]) is reachable. Appendix II delineates the mechanism for offline analysis and reachability assessment.

B. SBC Online EMI Mitigation

The SBC online problem is divided into two modes of operation as follows.

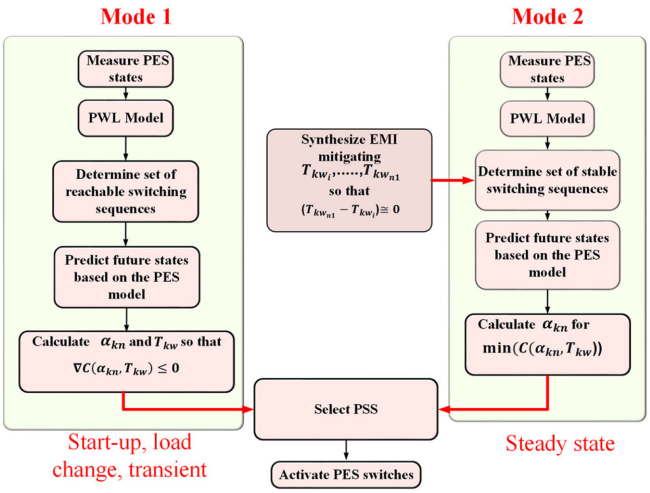

Fig. 4. Online SBC problem.

Mode 1: During the transient conditions like a start-up or sudden load change, an online cost function $C(\alpha_{\rm kn}, T_{\rm kw})$ is minimized with respect to $\alpha_{\rm kn}$ (n is a switching state in a given SS) and $T_{\rm kw}$ to synthesize a SS that guides the PES to its steady state.

Mode 2: During the PES steady state, as shown in Fig. 4, to satisfy the EMI standards, a certain value of the time horizon $T_{{\rm kw}_i} = T_{{\rm kw}_s} + \Delta T_{\rm kw} f(w_m t)$ that causes EMI mitigation is calculated and applied to the PES. The new value of $T_{{\rm kw}_i}$ is used in the online cost function $C(\alpha_{\rm kn}, T_{\rm kw})$ which is minimized with respect to $\alpha_{\rm kn}$ only to maintain voltage regulation. The cases will be described in more detail in the following subsections.

1) Online Prediction Model (Modes 1 and 2): For fast real-time execution of the SBC, an online prediction model of the PES is synthesized that closely matches the dynamics of the full-scale PES model used by the reachability analysis. The prediction model is synthesized using a discrete map of the PES, which is obtained by patching together the individual maps corresponding to each of the switching states. If the PES has h switching states in a reachable SS, the discrete prediction model for the $i+1$ sample can be synthesized as

$$\hat{x}\,(i+1) = \hat{A}_{knd}\hat{x}\,(i) + \hat{B}_{knd} \tag{1}$$

where $\hat{A}_{knd}$ and $\hat{B}_{knd}$ are the reduced-order PES matrices for online prediction and have been defined in Appendix III.

2) Cost Function Formulation (Modes 1 and 2): Next, a cost function, denoted by $C(\alpha_{\rm kn}, T_{\rm kw})$ is formulated and an optimal control problem is solved online to perform online performance control of the PES. The online optimization problem determines $\alpha_{\rm kn}$ and $T_{\rm kw}$ that minimizes the following cost function:

$$C\ (\alpha_{\rm kn}, T_{\rm kw}) = (\hat{x}^* - \hat{x}\,(i+1))^T\ P\,(\hat{x}^* - \hat{x}\,(i+1)) \tag{2}$$

given the constraints on PES states and bounds on $\alpha_{\rm kn}$ and $T_{\rm kw}$. In (2), P is a positive-definite matrix that provides scaling of the terms in the cost function. The optimization problem yields reachable SSs with optimal values of $\alpha_{\rm kn}$ and $T_{\rm kw}$ (i.e., $\alpha_{kn_{\rm opt}}$ and $T_{{\rm kw}_{\rm opt}}$) that are fed to the PES power stage.

3) Observer Design (Mode 1 and 2): Finally, if full-state feedback is not possible to preclude the need for a plurality of sensors for a higher order PES, a closed-loop state observer needs to be synthesized. If $\overline{\hat{x}}$ are the observed PES states, the expression for the closed-loop observer is given for the $(i+1)$ discrete sample by

$$\overline{\hat{x}}\,(i+1) = \overline{\hat{A}_{knd}}\overline{\hat{x}}\,(i) + \overline{\hat{B}_{knd}} \tag{3}$$

where $\overline{\hat{A}_{knd}}$ and $\overline{\hat{B}_{knd}}$ have been defined in Appendix III.

4) Constraints in SBC (Modes 1 and 2): Controllers [21]–[28] that solve an optimal-control problem like SBC, minimize cost functions as shown in Section II-A2.2, based on constraints and compute $\alpha_{\rm kn}$ and $T_{\rm kw}$. The constraints can be set on individual PES states like voltage, currents, and so on as in the form $\hat{x}(i) \leq x_{\max}$, where $x_{\max}$ denotes the limit set on the PES voltages, currents, or duty cycles. In this article, constraints have been used to reduce the PES DM and CM EMI peaks below EMI standards as follows.

1) For a generalized PES, the DM input current, which mainly contributes to the DM EMI peaks is used to create the DM EMI model. Similarly, the drain-to-source transitions of the PES devices that impact the charging the various parasitic capacitances of the PES set-up are used to form the CM EMI model.
2) For a PES operating in steady state with a time horizon $T_{{\rm kw}_s}$, (or constant switching frequency $T^{-1}_{{\rm kw}_s}$) the DM/CM current waveforms can be expressed as periodic time series (shown in Appendix IV) with C_{n_1} as the magnitude of the n_1th harmonic of $T^{-1}_{{\rm kw}_s}$. For this n_1th harmonic, if $C_{n_1}$is below the limiting harmonic peak $C_{{\rm EMI}n_1}$of the CISPR/EN 55022/32 Class-A EMI Standard [3] (that is, $C_{n_1} < C_{{\rm EMI}n_1}$), then $T_{{\rm kw}_s}$ is not changed.
3) However, if $C_{n_1} > C_{{\rm EMI}n_1}$ for the n_1th harmonic, then, a new time horizon $T_{\rm kw}$ is chosen that reduces PES EMI. It has already been established in Fig. 3, how two different SSs having different time horizons can lead to different EMI levels for a PES.

It is ensured that for EMI peaks corresponding to the new time horizon $T_{\rm kw}$ (say $C_{n_{1\rm new}}$, detailed in Appendix IV), $C_{n_{1\rm new}} < C_{{\rm EMI}n_1}$ is satisfied. The synthesis of this new time horizon $T_{\rm kw}$ is based on the basic principle laid forth by Van der Pol in [14], which demonstrates that when the frequency (inverse of the time horizon i.e., $T^{-1}_{\rm kw}$) of a signal, such as the DM/CM current in the present case, is periodically modulated, the individual spectral peaks of the original signal are reduced.

Fig. 5 shows the synthesis of this new $T_{\rm kw}$ for our case. It starts from a time horizon $T_{{\rm kw}_s}$ (or frequency $T^{-1}_{{\rm kw}_s}$), spans a certain time horizon $\Delta T_{\rm kw}$ (or frequency $\Delta T^{-1}_{\rm kw}$) on either side of $T_{{\rm kw}_s}$, and comes back to $T_{{\rm kw}_s}$. The periodicity of the $T^{-1}_{\rm kw}$ is taken as a sinusoid for ease of implementation. If the new time horizon $T_{\rm kw}$ contains h_1 switching states, the net reduction of the spectral peaks obtained depends on the values of $T_{\rm kw}$, the depth $\Delta T_{\rm kw}$, and $T_{\rm kw}/h_1$ [14]. All of these three parameters are shown in Fig. 5, while Appendix IV briefly shows the mathematical formulation for the method and calculation of EMI peaks C_{n_1} and $C_{n_{1\rm new}}$.

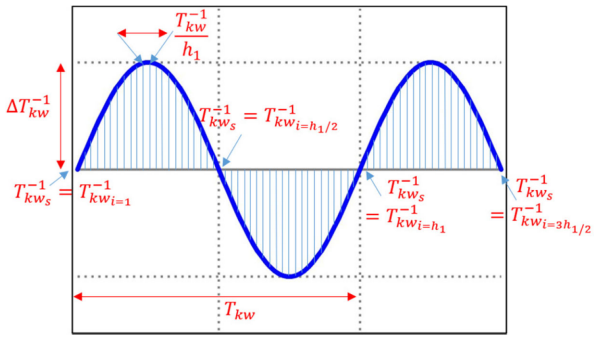

Fig. 5. Figure showing how T_{kw} is formed in steady state to reduce EMI spectrum.

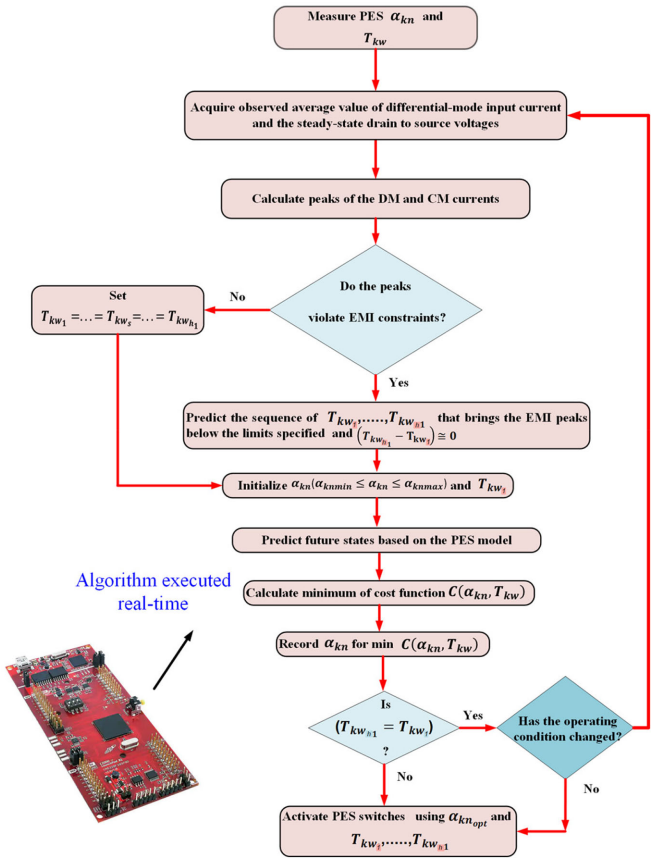

Fig. 6. Online SBC algorithm that performs conducted-EMI mitigation.

Fig. 6 shows the algorithm for online EMI mitigation. Depending on the present operating condition, and using an optimal framework, SBC calculates the EMI peaks of the PES using a DM/CM internal prediction model. If the peaks violate the standards, SBC calculates the new values of $T_{\rm kw}$, the depth $\Delta T_{\rm kw}$, and $T_{\rm kw}/h_1$, that can reduce PES EMI below the EMI standards, and applies this time horizon to the hardware PES. Subsequently, once the new $T_{\rm kw}$ to meet the EMI standards is fixed, SBC minimizes cost function $C(\alpha_{\rm kn}, T_{\rm kw})$ given in (2) to find the optimal $\alpha_{\rm kn}$ in the steady state. For any operating condition variation, the EMI peaks are recalculated, and the process repeats using the algorithm shown in Fig. 6.

III. SBC Implementation for EMI Mitigation of Ćuk–PES

For SBC, first, a full-scale model of the Ćuk–PES is synthesized offline that is used to perform a reachability analysis as elucidated in Section II-A1 to come up with a stable range of $\alpha_{\rm kn}$ and $T_{\rm kw}$ that can be used to solve the real-time SBC problem.

Next for the real-time part, Section II-A2.1 to II-A2.4 was followed for the PES. The real-time SBC problem is formulated for the Ćuk–PES into two steps as depicted in Modes 1 and 2. The detailed case illustration for Mode 1 for the Ćuk–PES, along with the nonlinear state observer design is depicted in [30], which encompasses cost function formulation and observer design guidelines for the PES up to the steady state. During the steady state, the cost function is modified as follows:

$$C_{\rm Mode-1}\ (\alpha_{\rm kn}, T_{\rm kw}) = \gamma_1 C_{vreg}\ (\alpha_{\rm kn}, T_{\rm kw}) + \gamma_2 (\Delta\alpha_{\rm kn}\ (i))^2 + \gamma_3 (\Delta T_{\rm kw}\ (i))^2 \tag{4a}$$

$$C_{\rm Mode-2}\ (\alpha_{\rm kn}, T_{\rm kw}) = \gamma_1 C_{vreg}\ (\alpha_{\rm kn}, T_{\rm kw}) + \gamma_2 (\Delta\alpha_{\rm kn}\ (i))^2 \tag{4b}$$

where

$$C_{vreg}\ (\alpha_{\rm kn}, T_{\rm kw}) = (G_p\ (V_{\rm ref} - V_{\rm out}\ (i)) + G_I \sum_j (V_{\rm ref} - V_{\rm out}\ (i))\ T_{\rm kw} - iL_1\ (i))^2 \tag{4c}$$

where the terms $IL_{\rm ref}$, $V_{\rm ref}, V_{\rm out}(i), iL_1(i)$ denote the input PES inductor current and output voltage references, output sensed voltage, and predicted inductor current sample, respectively. The weight-tuning factors δ_1, G_p, G_I, γ_1, γ_2, and γ_3 have all been synthesized based on guidelines defined in [30], [32]–[34]. Leading up to the steady state, SBC finds $\alpha_{\rm kn}$, and $T_{\rm kw}$ to make $\Delta C_{\rm Mode-1}(\alpha_{\rm kn}, T_{\rm kw}) < 0$. During steady state, SBC synthesizes $T_{\rm kw}$ depending on EMI mitigation, while $C_{\rm Mode-2}(\alpha_{\rm kn}, T_{\rm kw})$ is minimized with respect to $\alpha_{\rm kn}$ to maintain PES voltage regulation.

During the steady state in Mode 2, SBC synthesizes EMI-mitigating sequences, following the constraints on the EMI standards as delineated in Section II-A2.4. This helps in autonomous reduction of conducted EMI peaks of the PES. However, due to $T_{\rm kw}$ variation, the output voltage of the power supply gets affected negatively. Due to the low-frequency variation of the time horizon ($T_{\rm kw}$) introduced by the SSs in steady state to reduce EMI, low-frequency harmonics are reflected in the output voltage. This results in output voltage deviation from the steady-state value if SBC is applied without output voltage regulation. Hence, in steady state, SBC minimizes the cost objective $C_{\rm Mode-2}(\alpha_{\rm kn}, T_{\rm kw})$ to keep the low-frequency deviation within bounds. Fig. 7 explains the scenario by considering two consecutive SSs with different time horizons $T_{{\rm kw}_{i+1}}$ and $T_{{\rm kw}_{i+1}}$. Due to $T_{{\rm kw}_{i+1}} > T_{{\rm kw}_i}$, the output voltage ripple falls further for the second SS leading to a drop in average output voltage (say $V_{{\rm out}_{\rm avg}}$). To avoid this droop, SBC provides a steady-state

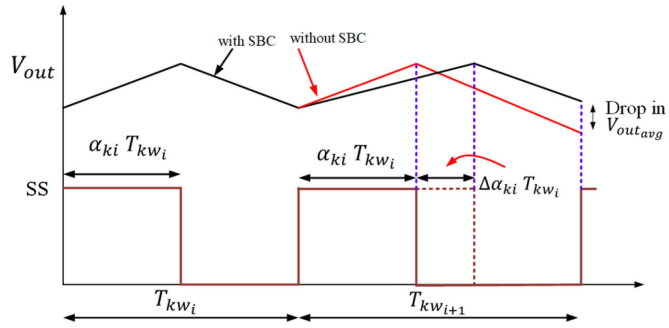

Fig. 7. Steady-state correction $\Delta\boldsymbol{\alpha_{ki}T_{kw_i}}$ provided by SBC using cost function (4) to reduce low-frequency output-voltage fluctuation due to time horizon variation for EMI mitigation.

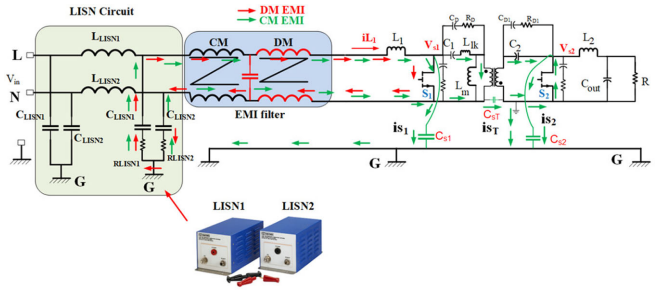

Fig. 8. CM and DM EMI propagation paths of the Ćuk–PES is shown with the LISN circuit.

correction $\Delta\alpha_{ki}T_{\mathrm{kw}_i}$ by minimizing (4b) to prevent output voltage deviation.

A. DM EMI Model Synthesis for Constrained Optimal Control

The CM- and DM-noise propagation paths of the Ćuk–PES are shown in Fig. 8. It shows the equipment under test (EUT) (i.e., the Ćuk–PES), any CM and DM filters that may be used for adhering to industrial EMI standards (CISPR/EN 55022/32 Class A and B conducted emissions for this case) and the LISN circuit which separates the EMI of the PES from the input power supply. The conducted CM noise generated by the GaN–FET transitions flows into the ground via the parasitic capacitances, and then picked up by the R_{LISN1} resistors back to the GaN–FETs. The main DM noise path is highlighted in red, while the CM noise paths have been highlighted in green.

The EMI measurements are taken using two LI-325C LISNs, named LISN1 and LISN2. The LISN circuits have also been delineated in Fig. 8. In the LISN circuit, $L_{\mathrm{LISN1}} = L_{\mathrm{LISN2}} = 5\ \mu$H, $C_{\mathrm{LISN1}} = 0.1\ \mu$F, $C_{\mathrm{LISN2}} = 1\ \mu$F, and $R_{\mathrm{LISN1}} = R_{\mathrm{LISN2}} = 50\,\Omega$. Over the frequency range of the EMI standards, L_{LISN1} and L_{LISN2} and C_{LISN1} and C_{LISN2} which are close to line to neutral (LN) in Fig. 8 are open circuits for LN; and the source V_{in} allows dc current to pass through to the PES. The other set of C_{LISN1} and C_{LISN2} close to the PES gives short circuit to the DM current and hence, impedances seen by the EUT between LG and NG (where G denotes ground/earth in Fig. 8 are R_{LISN1} and R_{LISN2}.

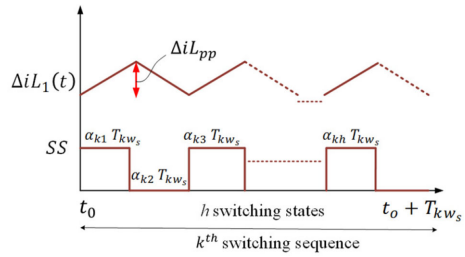

Fig. 9. Figure showing the steady-state SS without DM EMI peak reduction and the corresponding $\Delta\boldsymbol{iL_1(t)}$ in (5).

To derive the EMI peaks for DM and CM noise, the EMI filter in Fig. 8 is neglected. Now, in the Ćuk–PES, the (DM) triangular input current that mainly contributes to the DM EMI peaks is used for the DM model and is predicted by the closed-loop state observer as described in Section II-A2.3. The input inductor current is denoted by $iL_1(t)$ which consists of an average component (iL_{avg}) and a HF ripple component $(\Delta iL_1(\mathrm{t}))$, as illustrated in Fig. 9.

The DM input noise is primarily attributed to this time-varying ripple component $(\Delta\boldsymbol{iL_1(t)})$, which can be written in the form of a Fourier series as follows:

$$\Delta iL_1\ (t) = \sum_{n_1=1}^{\infty} C_{\mathrm{dm}} \exp^{\left(2\pi j\left(n_1 T_{\mathrm{kw}_s}^{-1}\right)t\right)} \tag{5}$$

where

$$C_{\mathrm{dm}} = \Delta iL_{\mathrm{pp}} * \frac{|\sin(\pi n_1 \alpha_{\mathrm{kn}})|}{n_1^2 \pi^2 \alpha_{\mathrm{kn}}\,(1-\alpha_{\mathrm{kn}})}. \tag{6}$$

In (5) and (6), C_{dm} is the amplitude of the n_1^{th} harmonic component of the DM EMI spectrum and ΔiL_{pp} is the magnitude of the peak-to-peak inductor-current ripple for particular operating conditions, also highlighted in Fig. 9. As discussed in Section II, A2.4, when the DM peaks (C_{dm} in (5)) of the Ćuk–PES exceed the DM EMI standards [3] (say C_{EMIdm}) i.e., $C_{\mathrm{dm}} > C_{\mathrm{EMIdm}}$, a new SS with a time horizon $T_{\mathrm{kw}} \in \{T_{\mathrm{kw}_i}, \ldots T_{\mathrm{kw}_s}, \ldots, T_{\mathrm{kw}_{h_1}}\}$ that can minimize the DM peaks of the Ćuk–PES below the EMI standards is chosen and applied to the PES. With this new SS, $\Delta iL_1(t)$ gets modified as follows:

$$\Delta iL_{1_{\mathrm{new}}}(t) = \sum_{n_1=0}^{\infty} \sum_{m_1=-\infty}^{\infty} C_{\mathrm{dm}_{\mathrm{new}}} \exp^{\left(2\pi j\left(n_1 T_{\mathrm{kw}_s}^{-1} + m_1 T_{\mathrm{kw}}^{-1}\right)t\right)} \tag{7}$$

where $C_{\mathrm{dm}_{\mathrm{new}}}$ are the reduced amplitudes of peaks of the DM EMI spectrum with the new T_{kw}. The derivation of $C_{\mathrm{dm}_{\mathrm{new}}}$ and the abbreviations used in (7) used have been derived and defined in Appendix IV. Fig. 10 shows $\Delta iL_{1_{\mathrm{new}}}(t)$ with the new SS that performs EMI mitigation.

B. Physical DM EMI Model Synthesis Considerations for Actual Hardware PES

To begin with, in the GaN–FET-based hardware prototype, the parasitic in the path of the DM current are not all accounted for while modeling the PES. The PES model precludes, for instance,

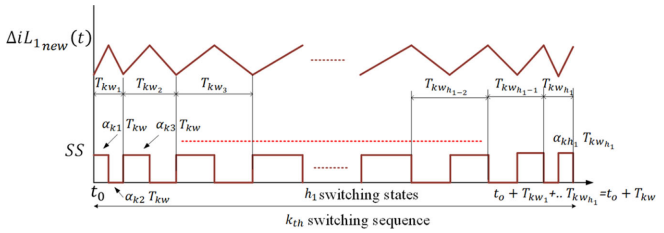

Fig. 10. Figure showing the new SS to reduce the DM EMI peak and the corresponding $\Delta iL_{1_{new}}(t)$ in (7).

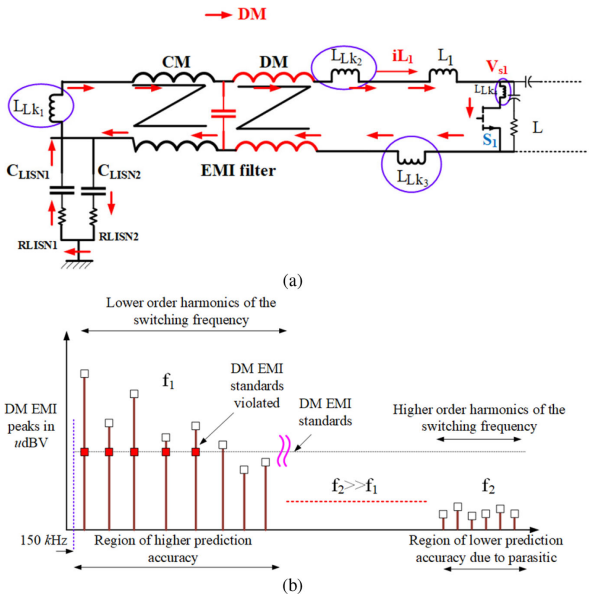

Fig. 11. Illustrations of (a) high-frequency parasitic that have not been considered for DM EMI model and (b) region in the DM EMI spectrum of the PES that violates the DM EMI standards.

HF DM leakage inductances and PCB trace inductances some of which have been lumped together and shown as $L_{LK_{12,..,4}}$ in Fig. 11(a). Hence, the DM peaks predicted based on the online PES model, may deviate from those obtained using the actual hardware prototype. However, it happens at very high frequencies since $L_{LK_{12,..,4}} \ll L_1$, and the DM EMI in the sidebands of the PES switching frequency is dominated by the inductor L_1. (since $L_1 + L_{LK_{12,..,4}} \cong L_1$). As illustrated in Fig. 11(b), the DM EMI peaks of a PES violate the EMI standards in the vicinity of the switching frequency (lower order harmonics of the switching frequency) where the DM peaks can be calculated with reasonable accuracy and the effect of the parasitic $L_{LK_{12,..,4}}$ inductances on the DM EMI peaks are negligible. Hence, since the DM harmonics due to parasitic $L_{LK_{12,..,4}}$ dominate the spectrum around the higher order of the switching frequency, they are not considered for prediction purposes.

We perform sensitivity analysis in hardware set-up on this assumption and thereby attempt to validate experimentally, that by the reduction of the DM EMI peaks in the proximity of the lower order switching sidebands, the DM EMI standards can be satisfied. Moreover, the inductor L_1 does not remain fixed in actual hardware prototype across wide operating power and

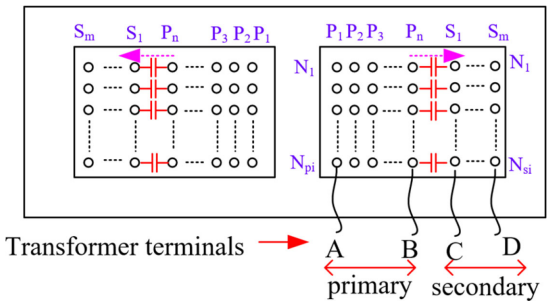

Fig. 12. Typical HF transformer structure with the parasitic interwinding capacitance that results in CM noise.

varies depending on the dc bias or the average input inductor current $\overline{iL_1(t)}$. The state observer in Section II-A2.3 predicts $\overline{iL_1(t)}$ and corrects the value of L_1 used in the online prediction model in real time.

Yet another issue pertains to the finite deadtime associated with the GaN–FET-based complementary devices of the Ćuk–PES. Hence, if the time allocated to a switching state in a SS is $\alpha_{\rm kn}$, then considering the deadtime, the allocation becomes $\alpha_{\rm kn} - \delta_{\rm deadtime}$. This affects the DM EMI peak prediction since the peaks predicted by (6) depend on the value of $\alpha_{\rm kn}$. Any modern industrial processor has deadtime modules and hence $\delta_{\rm deadtime}$ is preset and known in advance. Hence, the abovementioned steps were incorporated for better DM EMI prediction.

C. CM EMI Model Synthesis for Constrained Optimal Control

Unlike the DM current, the CM currents have more indeterministic coupling paths. Hence, to synthesize a CM PES model that can predict the CM peaks with reasonable accuracy, yet is simple enough for real-time optimal control, an analytical model is created for the main CM coupling paths, which have been shown in Fig. 8 for the isolated Ćuk–PES under consideration.

Two primary CM noise sources are primary (S_1) and secondary (S_2) GaN–FETs. The drain-to-source voltages of the GaN–FETs are denoted by V_{s_1} and V_{s_2}. The dv/dt caused by the FET switching transition charges the parasitic capacitances (say C_{s_1} and C_{s_2}, respectively) between the drain of the FET and the earth (G in Fig. 8) and this, in essence, constitutes the CM noise. The stray capacitance is mainly formed between the drain of the device and heatsink, as the insulating materials have considerable dielectric constant.

Another major CM EMI source is the parasitic interwinding capacitances between the primary and secondary windings of the transformer. In the Ćuk–PES, as shown in Fig. 8, the voltages on primary and secondary sides of the transformer are denoted by V_{T_p} and V_{T_s}, respectively. For nonunity turns ratio of the HF transformer and unequal voltage distribution across the windings, the switching transition of $V_{T_p} - V_{T_s}$ charges the interwinding capacitance to cause a displacement current from the primary to the secondary side of the transformer and the earth.

Fig. 12 shows a typical transformer structure where the primary and secondary sides have N_p and N_s turns, respectively,

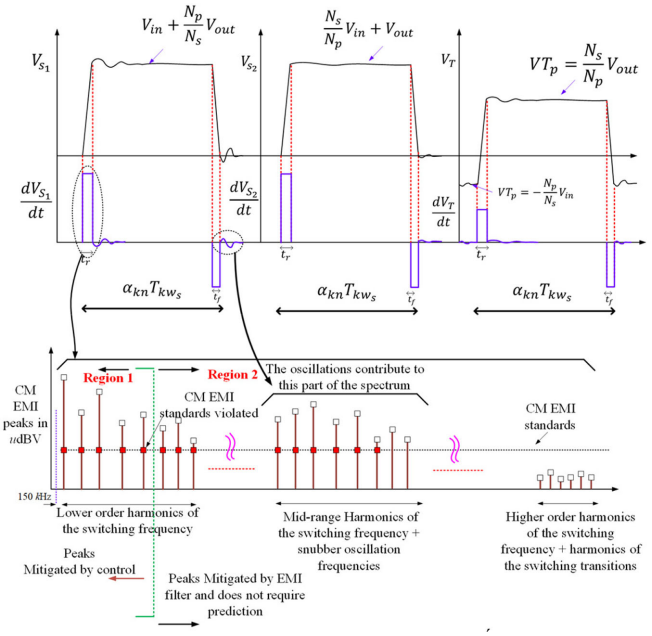

Fig. 13. Figure showing the switching voltages of the Ćuk–PES that mainly contribute to CM EMI. Also, the regions in the CM EMI control are shown.

and P_n and S_m layers, respectively. Due to the voltage difference between layer P_n and layer S_1, the interwinding capacitance between these two layers will result in a displacement current that can be written as $i_{S_T} = C_{\text{dis}}(N_{p_n} - N_s/N_{s_1})/2N_p dV_{T_p}/dt = C_{s_T} dV_{T_p}/dt$, where C_{dis} denotes the discrete capacitances between the primary layer P_n and secondary layer S_1, N_{p_n} and N_{s_1} are the number of turns in layer P_n and S_1, respectively, and $C_{\text{dis}}(N_{p_n} - N_s/N_{s_1})/2N_p$ is the total lumped interwinding capacitance. These three-time varying voltages V_{s_1}, V_{T_p}, and V_{s_2}, shown in Fig. 13, are the major contributors to the CM noise spectrum of the PES. Fig. 13 also shows the first derivatives of these time-varying voltages, which cause three CM currents i_{s_1}, i_{s_2}, and i_{s_T}. The currents, expressed as $i_{s_1} = C_{s_1} dV_{s_1}/dt$, $i_{s_2} = C_{s_2} dV_{s_2}/dt$, and $i_{s_T} = C_{s_T} dV_{T_p}/dt$, have been shown in Fig. 8. Since V_{s_1}, V_{T_p}, and V_{s_2} are all periodic, their derivatives which lead to the CM currents i_{s_1}, i_{s_2}, and i_{s_T} are also periodic and can be expressed using Fourier series like DM noise for peak prediction. The CM capacitors C_{s_1}, C_{s_T}, and C_{s_2} are usually very small in tens of pF and can be computed in detail by an impedance analyzer or using printed-circuit-board modeling for a given PES. The work in [13]–[35] highlight some of the peak-prediction procedure for CM EMI, by modeling PES in considerable detail. But, for our present application, such detailed models cannot be easily used in industrial digital signal processors (DSPs). Hence, we use some practical PES behavioral considerations and weave fine a data driven-analytical approach to predict CM noise for our application.

1) Physical CM EMI Model Synthesis Considerations for Actual Hardware PES

Fig. 13 shows the CM EMI spectrum, with the typical V_{s_1}, V_{T_p}, and V_{s_2} of a Ćuk–PES. The CM EMI spectrum consists of the switching-frequency components, the frequency components due to parasitic oscillations caused by the leakage of the transformer discharging into the device capacitance that rides on the V_{s_1}, V_{T_p}, and V_{s_2} signals. It also consists of the frequency components induced by the switching transition of the GaN–FETs. Even though the main paths of the CM EMI have been highlighted, the CM current can find indeterministic paths to the earth (G, shown in Fig. 8) and hence, the spectra cannot be predicted with accuracy all the way to the switching-transition components without exact knowledge of the practical-PES model.

In the CM EMI spectrum shown in Fig. 13, it is observed that the CM EMI standards for the Ćuk–PES are violated for lower order harmonics of the switching frequency and in the mid-range frequencies due to the parasitic oscillations induced by transformer leakage. So for the case under consideration, the peaks in the lower order harmonics are predicted and mitigated by control. We denote this region as Region 1. All the mid-range and higher order peaks are mitigated by designing a CM EMI filter by observing the experimental peaks in a spectrum analyzer during experimentation; hence, they will not be predicted. We denote this region as Region 2. By mitigating the lower order CM EMI peaks using control, the frequencies at which the CM EMI standards are violated are pushed to the higher end of the spectrum, which thereby reduces the size of the CM EMI filter.

Now, the CM current for the PES can be written in the form

$$i_{CM_{\text{total}}} = i_{s_1} + i_{s_2} + i_{s_T} \tag{8}$$

$$= C_{s_1}\frac{dV_{s_1}}{dt} + C_{s_2}\frac{dV_{s_2}}{dt} + C_{s_T}\frac{dV_{T_p}}{dt}. \tag{9}$$

In (9), dV_{S_1}/dt, dV_{S_2}/dt, and dV_{T_p}/dt are periodic waveforms, and hence $i_{CM_{\text{total}}}$ can be written in terms of a Fourier series as

$$i_{CM_{\text{total}}} = \sum_{n_1=1}^{\infty} C_{cm_{V_{s_1}}} \exp^{\left(2\pi j\left(n_1 T_{\text{kw}_s}^{-1}\right)t\right)} + \sum_{n_1=1}^{\infty} C_{cm_{V_{s_2}}} \exp^{\left(2\pi j\left(n_1 T_{\text{kw}_s}^{-1}\right)t\right)} + \sum_{n_1=1}^{\infty} C_{cm_{V_{s_T}}} \exp^{\left(2\pi j\left(n_1 T_{\text{kw}_s}^{-1}\right)t\right)} \tag{10}$$

$$= \sum_{n_1=1}^{\infty} C_{cm} \exp^{\left(2\pi j\left(n_1 T_{\text{kw}_s}^{-1}\right)t\right)}. \tag{11}$$

In (10), $C_{cm_{V_{s_1}}}$, $C_{cm_{V_{s_2}}}$, and $C_{cm_{V_{s_T}}}$ are the CM EMI peaks due to dV_{S_1}/dt, dV_{S_2}/dt, and dV_{T_p}/dt, respectively, and in (11), $C_{cm} = C_{cm_{V_{s_1}}} + C_{cm_{V_{s_2}}} + C_{cm_{V_{s_T}}}$. Here the process of derivation of only $C_{cm_{V_{s_1}}}$ is delineated and the derivations of $C_{cm_{V_{s_2}}}$ and $C_{cm_{V_{s_T}}}$ are similar.

From Fig. 13, one observes that V_{s_1} transits between zero and the value given by $V_{\text{in}} + N_p/N_s V_{\text{out}}$. Hence, if the rising and falling edges of V_{s_1} are given by t_r and t_f, then, the function

$C_{s_1} dV_{s_1}/dt$ can be written as $C_{s_1} \frac{V_{\text{in}} + \frac{N_p}{N_s} V_{\text{out}}}{tr}$ between zero to t_r, and zero in between t_r to $\alpha_{\text{kn}} T_{\text{kw}_s} - t_f$, $C_{s_1} \frac{V_{\text{in}} + \frac{N_p}{N_s} V_{\text{out}}}{t_f}$ between $\alpha_{\text{kn}} T_{\text{kw}_s} - t_f$ to $\alpha_{\text{kn}} T_{\text{kw}_s}$, and zero in between $\alpha_{\text{kn}} T_{\text{kw}_s}$ to T_{kw_s}. Hence, the periodic function can be broken down into Fourier components and the peaks of $C_{s_1} dV_{s_1}/dt$ denoted by $C_{cm_{V_{s_1}}}$ are expressed by the following:

$$C_{cm_{V_{S_1}}} = \sqrt{A^2_{cm_{V_{S_1}}} + B^2_{cm_{V_{S_1}}}} \tag{11a}$$

$$A_{cm_{V_{S_1}}} = \left(\frac{2\left(T_{\text{kw}_s} a_2 \left(\frac{\sin(y)}{T_{\text{kw}_s}} \right) - \frac{\sin(t_f + y)}{T_{\text{kw}_s}} \right)}{2\pi p_1} + z \right) \Big/ T_{\text{kw}_s} \tag{11b}$$

$$B_{cm_{V_{s_1}}} = \frac{-(2\left(T_{\text{kw}_s} a_2 \left(\frac{\cos(y)}{T_{\text{kw}_s}} \right) - \frac{\cos(t_f + y)}{T_{\text{kw}_s}} \right))}{2\pi p_1} - z)/T_{\text{kw}_s} \tag{11c}$$

$$y = 2\pi n_1 \left(t_r + T_{\text{kw}_s} \alpha_{\text{kn}} \right) \tag{11d}$$

$$a_1 = C_{s_1} \frac{V_{\text{in}} + \frac{N_p}{N_s} V_{\text{out}}}{tr}, a_2 = C_{s_1} \frac{V_{\text{in}} + \frac{N_p}{N_s} V_{\text{out}}}{t_f} \tag{11e}$$

$$z = \frac{T_{\text{kw}_s} a_1 \sin((2\pi n_1 t_r)/T_{\text{kw}_s})}{2 n_1 \pi}. \tag{11f}$$

Even though C_{s_1}, C_{s_T}, and C_{s_2} can be calculated via use of impedance analyzer and PCB modeling based approaches [36], the process can prove tedious for different hardware setups and transformers. Hence, an easier experimental data-driven approach is used here for estimating the parasitic capacitances. For different V_{in} and V_{out} of the Ćuk–PES, obtained for the experimental PES hardware using a spectrum analyzer, the real-time peaks of the CM EMI are measured. Let the experimental peaks be denoted by $C_{cm\text{exp}_i}$ and the ones calculated from analytical model be C_{cm_i}. Now, using the simple algorithm delineated in Fig. 14, we tune the values of C_{s_1}, C_{s_T}, and C_{s_2} that minimizes the function $(|C_{cm\,expi} - C_{cm_i}|)$. As shown in Fig. 14, the order of the harmonic n_1 for the CM spectrum up to which the EMI peaks will be mitigated by control is chosen such that the error in the prediction of these peaks is below a programmable predefined threshold ε.

Finally, following the methodology in Section II-A2.4, when the CM peaks (of the Ćuk–PES) C_{cm} in (11) exceed the amplitudes $(C_{\text{EMI}cm})$ of the CM harmonics specified by the EMI standards [3] (i.e., $C_{cm} > C_{\text{EMI}cm}$), a new SS with a time horizon $T_{\text{kw}} \in \{T_{\text{kw}_1}, \ldots T_{\text{kw}_s}, \ldots, T_{\text{kw}_{h_1}}\}$ that can minimize the CM peaks to an acceptable level are chosen. When the new SS is applied, $i_{CM_{\text{total}}}$ modifies to the following form:

$$i_{CM_{\text{total}_{\text{new}}}}(t) = \sum_{n_1=0}^{\infty} \sum_{m_1=-\infty}^{\infty} C_{cm_{\text{new}}} \exp^{\left(2\pi j \left(n_1 T^{-1}_{\text{kw}_s} + m_1 T^{-1}_{\text{kw}}\right) t\right)} \tag{12}$$

where $C_{cm_{\text{new}}}$ are the reduced amplitudes of peaks of the CM EMI spectrum. Derivation of $C_{cm_{\text{new}}}$ and the abbreviations used in (12) have been provided in Appendix IV.

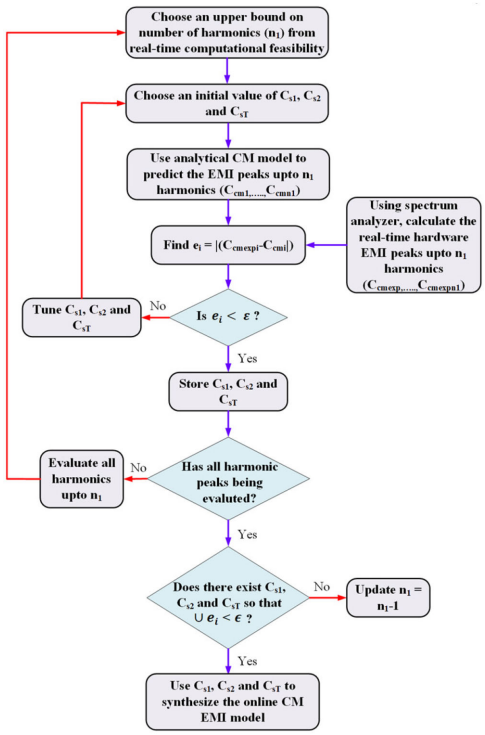

Fig. 14. Offline algorithm in MATLAB to compute the value of common mode capacitors C_{s_1}, C_{s_T}, and C_{s_2} based on experimental data. ε denotes a programmable predefined threshold.

IV. Results

The section is organized as follows.

1) First, the hardware set-up is explained in Section II-A1.
2) Then, Section II-A2 delineates the time-domain experimental validation of the proposed approach in controlling the PES in terms of the steady state and transient waveforms. In Mode 1, SBC synthesizes SSs that guide the PES to steady state, and in Mode 2 does steady-state regulation and EMI mitigation.
3) Section II-A3 shows how SBC autonomously mitigates DM EMI, and its effect on the DM filter size in the PES.
4) Section II-A4 shows CM EMI mitigation and the subsequent CM EMI size reduction.
5) Finally, it is experimentally demonstrated in Section II-A5 how the EMI mitigating SBC affects PES efficiency compared to traditional EMI filter losses. It also shows SBC based low-frequency distortion control results.

A. Hardware Prototype and Set-Up Description

The hardware prototype consisting of the higher order GaN–FET-based Ćuk–PES is shown in Fig. 15(a). The PES hardware prototype is used to perform the EMI experiments using the setup depicted in Fig. 15(b) and (c).

The SBC algorithm is implemented on a low-cost dual-core TMS320F28379D DSP (LaunchXL-F28379D) using code composer studio version 8, and the SS, with the allocated switching states (α_{kn}) and time horizon (T_{kw}), is used to drive the

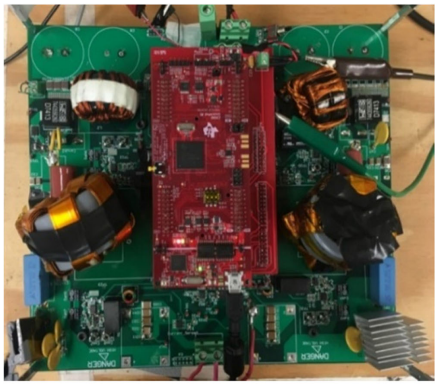

(a)

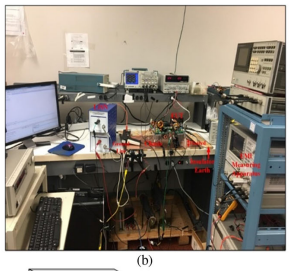

(b)

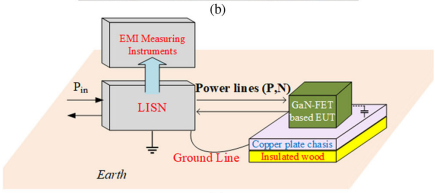

(c)

Fig. 15. (a) PCB realization of the GaN-FET-based Ćuk-PES. (b) PES experimental set-up for performing the EMI tests. (c) Set-up for conducted emission measurement.

TABLE I
POWER-STAGE PARAMETERS FOR THE ĆUK–PES

Input voltage range (V_{in})	Output voltage range (V_{out})	Input inductance (L_1)	Output inductance (L_2)	Input capacitance (C_{in})
30-60 V	0-90 V	50 μH	100 μH	4.4 μF
Output capacitance (C_{out})	Input blocking capacitance (C_1)	Output blocking capacitance (C_2)	Switching frequency ($1/T_s$)	Transformer turns ratio (N)
30 μF	6.8 μF	1.5 μF	100-250 kHz	2

GS66508B GaN–FET-based Ćuk–PES operating at the maximum power of 350 W. The power-stage parameters used are provided in Table I. The detailed hardware design is discussed in [1]. The PCB layout in terms of the power, control, and gate loops have been further optimized, than that discussed in [1], to minimize stray CM EMI noise. The EMI measurements are taken using LI-325C LISNs and 4395A Agilent Network/Spectrum/Impedance Analyzer. The set-up is implemented taking into consideration CISPR/EN 55022/32 Class A and B conducted emissions measuring standard.

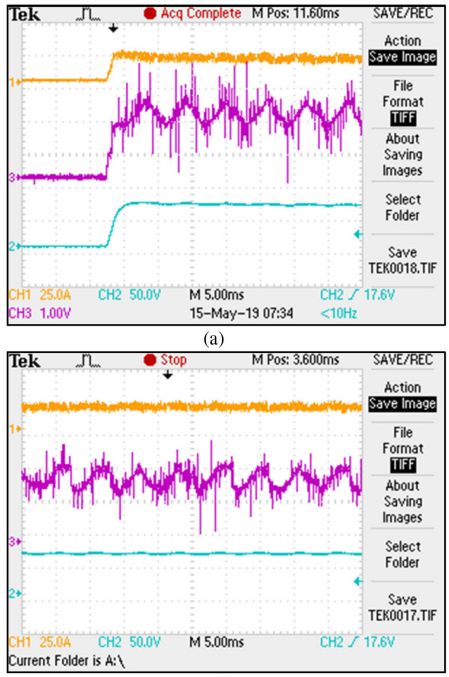

(a)

(b)

Fig. 16. (a) The PES start-up response. (b) The PES steady-state response. Both the results are taken at 350 W. The traces from top to bottom show the input PES current, $\alpha_{k1}T_{\rm kw}$ variation (plotted as DAC output), and the output voltage of the PES.

B. PES Autonomous EMI Mitigation

The online SBC consists of two parts:

1) Mode 1-operation during transient operation leading up to the steady state where SBC determines the switching states ($\alpha_{\rm kn}$) and time horizon ($T_{\rm kw}$) on the fly via minimization of the cost function defined in (4a).

2) Mode 2-operation in the steady state. Here, the switching states ($\alpha_{\rm kn}$) of the SS are synthesized to perform voltage regulation via minimization of the cost function defined in (4b), while $T_{\rm kw} \in \{T_{{\rm kw}_1}, \ldots\ldots, T_{{\rm kw}_{h_1}}\}$ that does EMI mitigation at the specific PES operating condition is found out and applied to the PES. The algorithm outlined in Fig. 6 is followed.

Fig. 16(a) and (b) shows the experimental PES start-up and steady-state time-domain response obtained with SBC at 350 W.

Fig. 17(a) and (b) further shows the PES response for a step change in reference power for the PES from 350 to 20 W. The $\alpha_{\rm kn}T_{\rm kw}$ variation (plotted as DAC output) is of importance here. In Fig. 17, the PES reaches steady-state power of 350 W in Region 2 via Region 1. Then the operating condition shifts to 20 W in Region 4 via Region 3. The regions are so chosen that EMI standards [3] are violated in Region 2 and not in Region 4.

As shown in Fig. 17(b), at 350 W, SBC in Mode-2 synthesized a SS ($\alpha_{\rm kn}$ and $T_{\rm kw} \in \{T_{{\rm kw}_1}, \ldots\ldots, T_{{\rm kw}_{h_1}}\}$) that does EMI mitigation in Region 2 and minimizes the cost-function in (4b). In Region 2, SBC varied the $\alpha_{\rm kn}T_{\rm kw}$ to keep output voltage constant as shown in the middle trace in Fig. 17(b).

On changing the operating point to 20 W, SBC stops synthesizing EMI mitigating sequence in Region 3 and minimizes the cost function in (4a) to reach the new steady state in Region 4.

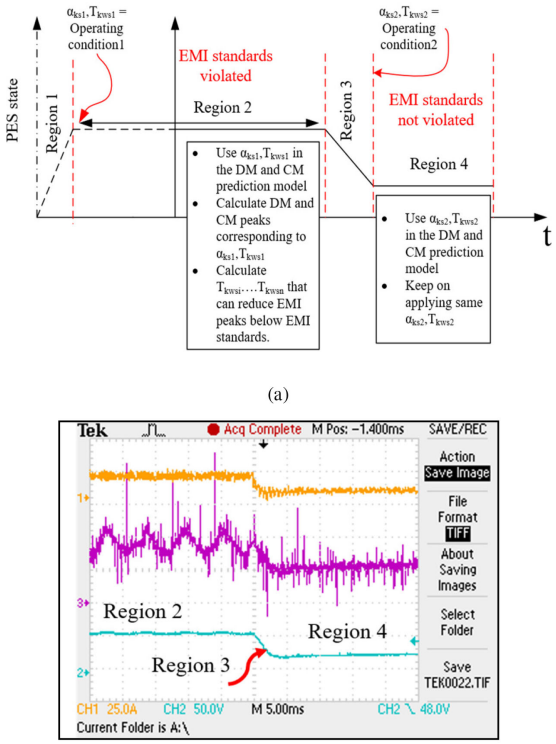

(a)

(b)

Fig. 17. (a) and (b) Automatic adjustment of the switching sequences by SBC on change of operating condition. The traces from top to bottom in (b) show the input PES current, $\alpha_{\rm kn}T_{\rm kw}$ variation (plotted as DAC output), and the output voltage of the PES.

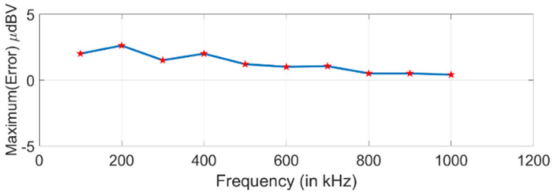

Fig. 18. Worst-case error in DM peak prediction due to the hardware/PES model mismatches as discussed in Section III-A1.1.

On reaching the new steady state at significantly lower power, SBC using the algorithm in Fig. 6 does not perform EMI mitigation since EMI standards [3] are not violated. The $\alpha_{\rm kn}T_{\rm kw}$ variation in trace-2 shows that the SBC, hence, adapts its SS ($\alpha_{\rm kn}$ and $T_{\rm kw} \in \{T_{\rm kw_1}, \ldots T_{\rm kw_s} \ldots, T_{\rm kw_{h_1}}\}$) autonomously in the steady state depending on the change of operating condition.

C. PES DM EMI Mitigation With Sensitivity Analysis

Fig. 18 shows the maximum error (across wide operating conditions) between the experimental and analytical DM EMI peaks. The online prediction model for DM EMI is made by using up to 10 DM peaks above the EMI limits of 150 kHz. This is because: 1) the DM EMI standards are usually violated below this range, as discussed in Section III-A1.1, 2) the error in DM peak prediction in this region is appreciably low (usually less than 2% of the steady-state peaks).

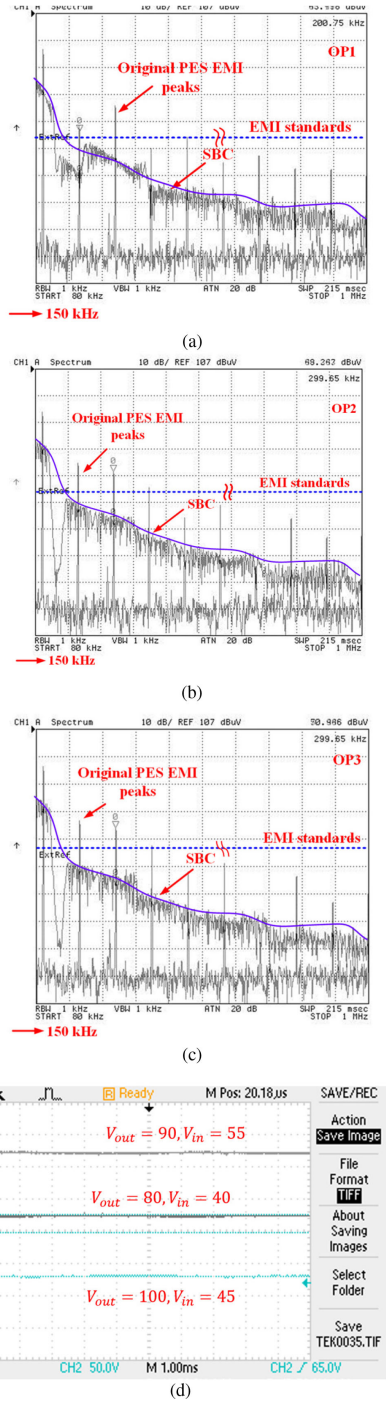

Fig. 19. Experimental PES spectrum showing the DM EMI peak reduction using SBC across various operating conditions as (a) $\boldsymbol{V_{\rm in}}$= 45 V, $\boldsymbol{V_{\rm out}}$= 100 V, and $\boldsymbol{P_{\rm out}}$ = 300 W (OP$_1$), (b) $\boldsymbol{V_{\rm in}}$= 40 V, $\boldsymbol{V_{\rm out}}$= 80 V, and $\boldsymbol{P_{\rm out}}$ = 200 W (OP$_2$), and (c) $\boldsymbol{V_{\rm in}}$= 55 V, $\boldsymbol{V_{\rm out}}$= 90 V, and $\boldsymbol{P_{\rm out}}$ = 210 W. (d) Figure showing the output voltages for the operating points.

Fig. 19 shows the SBC-based DM EMI-mitigation across various operating conditions of the PES and plots the output voltage corresponding to those points. Fig. 19(a)–(c) shows three operating points of the PES, chosen at random as OP1: $V_{\rm in}$= 45 V, $V_{\rm out}$= 100 V, $P_{\rm out}$ = 300 W, OP2: $V_{\rm in}$= 40 V, $V_{\rm out}$= 80 V, $P_{\rm out}$ = 200 W OP3: $V_{\rm in}$= 55 V, $V_{\rm out}$= 90 V, and $P_{\rm out}$ = 210 W.

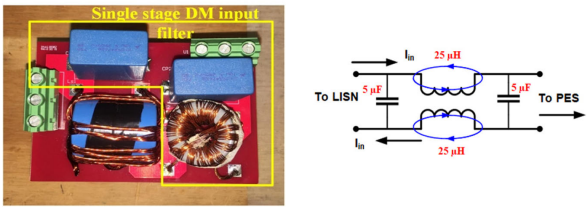

Fig. 20. DM EMI filter at the input side to suppress the DM noise peaks that are mitigated by SBC.

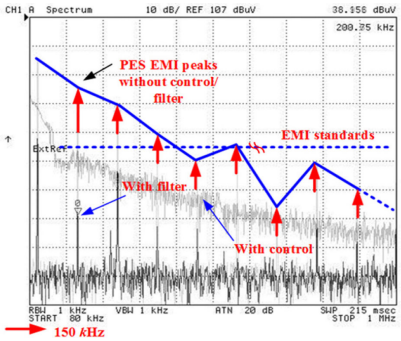

Fig. 21. The comparative analysis of the EMI filter based peak reduction (bottom trace), SBC based peak reduction (middle trace), and original EMI DM peaks without EMI filter and without EMI mitigating SBC (top trace-red). The EMI standards are specified in blue.

In all these three cases, the effect of the application of the SBC with DM EMI mitigating sequences (the reduced peaks with higher EMI floor in Fig. 19) is compared against SBC without DM EMI mitigation (the isolated/islanded discrete DM EMI peaks in Fig. 19). On violation of the EMI standards [3] in the steady state, SBC selects a new value of $T_{\rm kw}$, the depth $\Delta T_{\rm kw}$ and $T_{\rm kw}/h_1$ (refer to Fig. 5) that can reduce DM EMI peaks below the DM EMI standards leading to an entirely autonomous DM EMI mitigating system. A small safety margin is used to account for the PES model/hardware DM EMI peak mismatches shown in Fig. 18. Fig. 19(d) shows the output voltage of the PES for the three operating points.

1) DM EMI Size Mitigation: SBC provides programmable DM EMI suppression which reduces the size of EMI filter and in some cases precludes the need for it as is the case with the PES under consideration. For visual depiction and quantitative analysis, an EMI filter to suppress the DM peaks is designed following [4], [6], [9] for the worst-case operating point for DM EMI for the Ćuk–PES. The designed EMI filter is shown in Fig. 20. The DM EMI inductor has to carry the full input current and is designed accordingly by keeping the inductance less and capacitance higher as specified in [9] for higher input currents. The inductor/capacitor combination is hence determined to be 50 and 5 μF, respectively, for providing the attenuation required with some overcompensation.

For the same worst-case DM EMI, Fig. 21 provides a comparative analysis via experimental results, showing the following conditions:

1) EMI peak suppression by DM EMI filter designed;
2) SBC based DM EMI mitigation;
3) the original unsuppressed DM EMI peaks.

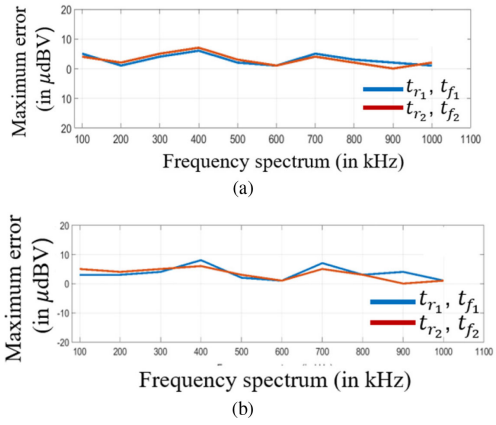

Fig. 22. (a) Worst-case error in predictions for the CM EMI for hardware PES set-up 1 for two different values of switching transitions. (b) Worst-case error in predictions for the CM EMI for hardware PES set-up 2 for two different values of switching transitions. The worst-case error never exceeds $\varepsilon = 8$ μdBV.

Thus, SBC with DM EMI mitigating sequences eliminated the need for the DM EMI filter shown in Fig. 20 for the Ćuk–PES. This also resulted in a decrease in the weight of the PES by 0.45 kg.

D. PES CM EMI Mitigation With Sensitivity Analysis

Since CM cases are heavily dependent on indeterministic parasitic coupling paths, an analytical model was created, and experimental data was used to find reasonable C_{s_1}, C_{s_T}, and C_{s_2} to reduce PES model/hardware inaccuracies and a CM model for the PES was formed. For finding feasible values of the common mode capacitors using the algorithm in Fig. 14, $\varepsilon \leq 10$ μdBV was used. The methodology is delineated in detail in Sections III-A2. Fig. 22(a) shows the efficacy of the CM EMI peaks predicted by the CM model so constructed by plotting the maximum error ($|C_{cmexpi} - C_{cm_i}|$) for wide range of operating conditions.

C_{cmexpi} denotes the real-time CM EMI peaks of the hardware PES, while C_{cm_i} are the peaks predicted by the CM EMI model. Fig. 22(a) also shows the error for two different values of switching transitions t_r (rise time) and t_f(fall time), namely $t_{r_1} = 30$ ns, $t_{f_1} = 10$ ns, and $t_{r_2} = 80$ ns, and $t_{f_2} = 30$ ns. The rise and fall times for the second case is chosen to show the validity of the proposed approach for devices with slower transitions respective to GaN–FETs like Si MOSFETs. Thus, the proposed CM EMI model works for different dv/dt transitions, as well with reasonable accuracy.

Because CM cases are parasitic modeling dependent, Fig. 22(a) shows the error ($|C_{cmexpi} - C_{cm_i}|$), for a different PES hardware set-up to show the sensitivity of the CM EMI model. Instead of GS66508B GaN–FETs, a previous generation GaN–FET board using GS66508P GaN–FETs (same rating) was used. The previous generation GaN–FET board has changes in layout, gate drive design (isolated/nonisolated), and an extra LC snubber on the primary side. Also, the transformer structure was varied by using different number of layers for the primary and secondary windings, keeping the turns ratio and number of turns on each side same. Like Fig. 22(a) and (b) also plots

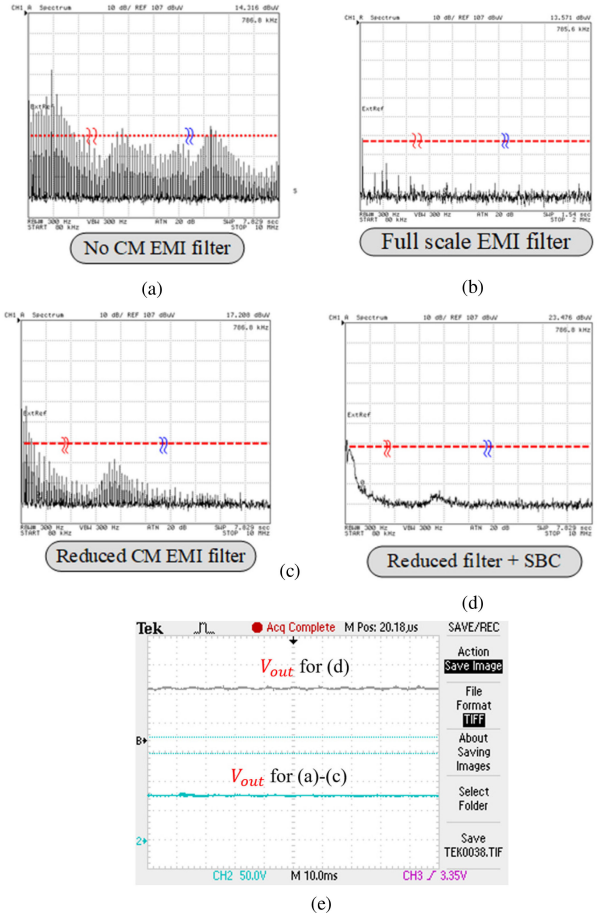

Fig. 23. (a) The CM EMI spectrum of the Ćuk–PES for SBC without EMI mitigating sequences. (b) Figure shows the CM EMI spectrum of the Ćuk–PES for SBC without EMI mitigating sequences and full-scale EMI filter. (c) The CM EMI spectrum of the Ćuk–PES for SBC without EMI mitigating sequences and reduced-size EMI filter. (b) The CM EMI spectrum of the Ćuk–PES for SBC with EMI mitigating sequences and reduced-size EMI filter. The CM EMI standards [3] have been highlighted in red. (e) Output voltages of the above four cases have been compared.

$|C_{cmexpi} - C_{cm_i}|$ for two different values of dv/dt transition rate.

Now, with reference to Fig. 13, we hence define two regions.

1) Region 1: In this region, SBC is synthesized in a predictive manner due to reasonably accurate predictions of the CM EMI. Any CM noise peaks below the 10th harmonic of the switching frequency will be addressed by SBC.

2) Region 2: In this region, the peaks will not be predicted. A CM EMI filter is designed based on guidelines of [9], which will address the CM EMI peaks.

Fig. 23 shows the experimental results obtained by SBC using the online CM EMI model. Fig. 23(a) shows the CM EMI spectrum of the Ćuk–PES for SBC without EMI mitigating SSs for the worst-case CM EMI point. Referenced to Fig. 13, the spectrum is dominated by the lower order harmonics of the switching frequency and mid-range harmonics due to parasitic oscillations.

Fig. 23(b) shows the CM EMI spectrum of the Ćuk–PES for SBC without EMI mitigating sequences but with a full-scale CM EMI filter [9]. The spectrum meets the CM standards across the entire range. Fig. 23(c) shows the CM EMI spectrum of the Ćuk–PES for SBC without EMI mitigating sequences and reduced-size EMI filter. The EMI filter is designed for higher cut-off frequency thereby reducing the size. However, the CM EMI peaks still violate the standards around the lower order harmonics. Fig. 23(d) then shows the spectrum of SBC with EMI mitigating SSs which brings all the peaks below the EMI standards. The output voltage for the above four cases has been shown in Fig. 23(e).

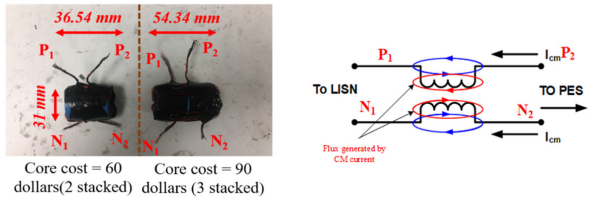

Fig. 24. Comparative figure showing the designed full-scale and reduced-order EMI filter for the worst-case CM EMI mitigation. The EMI filter is designed with high-cost high permeability FINEMET cores.

Fig. 24 shows the reduction in EMI filter size and cost due to SBC-based EMI mitigation. HITACHI FINEMET cores with very high permeability have been used as core materials for CM filter design. For the full-scale EMI filter for Fig. 23(b), three FINEMET cores each costing 30 dollars [39] have been stacked to create the CM EMI filter of 16 mH considering the window area for the required number of turns. The CM filter did not consist of any CM capacitor. For the reduced size CM EMI filter for Fig. 23(c) and (d), two cores are stacked together to create 5 mH of CM inductance in conjunction with SBC-based EMI mitigation to satisfy the CM standards. This results in 33.33% reduction in core cost for the CM inductor design. The FINEMET cores used for the CM filter have very high permeability thereby providing high inductance value in limited size and weight. Hence, CM filter size reduction does not lead to an appreciable specific weight variation of the PES. However, the use of alternative low-cost low-permeable cores for CM filter will lead to appreciable specific weight decrement of a PES due to huge inductance of CM filters.

E. Low-Frequency Distortion, PES Efficiency, and Effect of ADC Resolution and Delays

1) Low-Frequency Distortion: As shown in Fig. 7, $T_{\rm kw}$ variation in steady state to perform EMI mitigation results in output voltage fluctuation. SBC systematically controls $\alpha_{\rm kn}T_{\rm kw}$ of a SS to keep the low-frequency deviation within bounds. Fig. 25(a) shows a comparative analysis of two situations to validate it experimentally.

The grey trace signifies the scenario (Case 1) when the steady-state EMI mitigating sequences are applied without performing output voltage regulation using SBC in steady state with capacitor $C_2 = 10\ \mu$F, in Fig. 25(b). The output voltage fluctuations are considerable.

The yellow trace signifies the scenario when the SBC minimizes a cost-objective (4) of the output voltage fluctuations even in steady state, but with a slightly bigger capacitor $C_2 = 30\ \mu$F as shown by the comparative analysis in Fig. 25(b). It causes

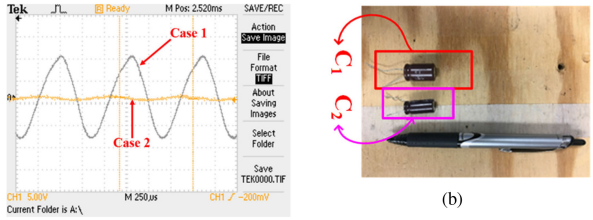

(a) (b)

Fig. 25. (a) Comparison of the output voltages in Cases 1 and 2. Case 1 can be alternatively thought of as a scenario when the output voltage regulation feature of the control is disabled. The vertical scale signifies 5 V/div and the average output voltage is 90 V. (b) Output capacitor size increase used by SBC for negligible output voltage deviations.

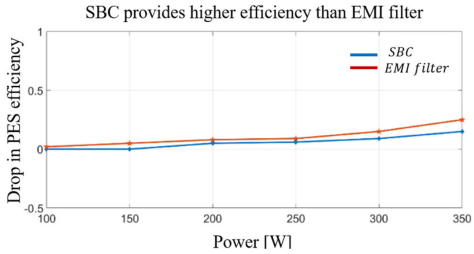

Fig. 26. The decrease of EMI filter size using SBC does not come at a price of decreased PES efficiency.

negligible output voltage deviations. From a power density and specific weight perspective, the capacitor size increment for the Ćuk–PES is less considered to EMI filter size reduction.

2) PES Efficiency: In addition to the decreased EMI size and autonomous EMI mitigation, SBC has a positive effect on the operating efficiency of the PES. With an operating point of $V_{\rm in}=$ 30 V, $V_{\rm out}=$ 90 V, the power throughput of the PES is gradually increased by increasing the load for the below scenarios:

First, without the CM/DM EMI filter, SBC is used to synthesize the SSs, both transient and steady state. In transient, SBC performed optimization of $\alpha_{\rm kn}$ and $T_{\rm kw}$ to provide the desired response. Second, in steady state, the SBC held on to the steady-state output value providing good regulation.

1) Second, the first case is repeated with the full-scale EMI filter [5], [9] to do the DM/CM EMI peak reduction.

Third, instead of using the full-scale EMI filter, SBC reduces DM and CM EMI peaks and uses a reduced-order CM filter. SBC also provides on-time variation of the SSs to keep output voltage constant.

Fig. 26 shows the difference in efficiencies of case 1 with that of cases 2 and 3. SBC based EMI reduction provided better efficiency results than the case with EMI filter, even for such moderate power systems.

3) Comments on Sensors, ADC Acquisition and Delays, and Execution Time: SBC uses a comprehensive HF PES model to predict the EMI peaks for a PES for different operating conditions. It uses the EMI peaks to solve a constrained online optimal problem. For DM EMI, an open-loop HF PES model was used with safety margins to account for PES model/hardware mismatches, while for CM EMI a data-driven HF analytical model was formed. Both the models were used by SBC to reduce

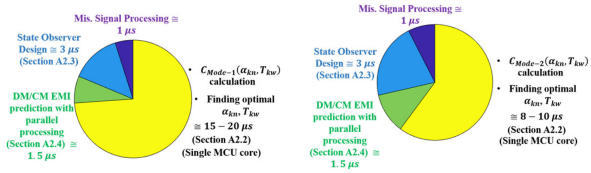

(a) (b)

Fig. 27. Figure execution time and/or time-breakdown for the overall SBC control in Modes 1 (a) and 2 (b) of operation, respectively.

PES EMI autonomously, as shown experimentally. Alternate to the approach taken, the EMI peaks could have been measured real-time for SBC. For a case illustration for the CM EMI, for $T_{\rm kw_s} = 10$ μs, to capture the components up to 10th to 15th harmonic would have necessitated greater than 10 MHz ADC sensing. Additionally, computation of n-point FFT to calculate the EMI peaks for CM/DM current would have gone beyond the computational capabilities of low-cost digital processors.

Hence, using internal HF DM/CM models preclude the need for extremely high-bandwidth ADC sensing and saves DSP computation time. The real-time EMI peaks calculated depends on HF EMI model and steady-state values of the $V_{\rm in}$ and $V_{\rm out}$ voltage sensors, using (5) and (11). The voltage sensors are low-bandwidth and acquired digitally using the 16-bit ADCs of F28379D, at a sampling rate of 2 MHz. Considering ADC acquisition of $V_{\rm in}$ voltage sensor, decreasing the ADC bit resolution to 12 and 8 instead of 16, would lead to slight errors in EMI peak prediction of 0.03 and 0.69 μdB, respectively, and deteriorated control performance.

The execution time of the SBC also affects control performance. For processors with faster instruction cycle time, SBC execution takes less computational time, which positively affects control performance in areas like output state regulation etc. because of the increased resolution of the control actions that can be achieved. Hence, for slow instruction cycle at a high switching frequency, to close the control loop in each switching cycle, the control resolution will become poor, thereby negating the effectiveness of such controllers. For the TMS320F28379D MCU, which is a high-performance industrial DSP for general power converter control, the execution time breakdown for the overall SBC control in Modes 1 and 2 of operation has been shown in Fig. 27.

V. Conclusion

SBC that does EMI mitigation is discussed in this article. SBC, in addition to synthesizing reachable sequences that ensure global stability for the PES, does DM and limited CM EMI mitigation.

The importance of SBC is as follows.

1) By use of comprehensive HF PES model, SBC precludes need for complex sensing and high bandwidth ADCs, which simplifies PES design.
2) Second, it reduces and, in some cases, precludes the need for EMI filters that negatively affects the power density and efficiency of the PES.

3) It gives high programmability to PES design. A PES operating at 10%–50% of the rated condition does not necessitate bulky EMI filter to do overcompensation of EMI peaks at lighter loads. At higher power levels, when only the control will not be enough to mitigate the EMI peaks, an EMI filter-control in integrated combination may provide good flexibility.

Moreover, SBC does perfect on-time regulation of the SSs which limits the slower-scale deterioration as evident from the experimental results. This approach is particularly useful for the ever-evolving fast-transition devices like the GaN FETs with high dv/dt. Devices like these can be switched at higher frequencies under high power due to their low device capacitances, yet higher voltage and current ratings. The high dv/dt of these devices also lead to lower switching losses at higher frequencies. However, operation at high power at higher frequencies may lead to bulky EMI filter or higher order EMI filter to provide the desired attenuation. This is because of the strict contemporary EMI standards. Even though a higher order EMI filter yields a robust option to meet the EMI targets and provide higher cut-off rate, it may affect the stability margin of a PES negatively in nonminimum phase systems which can impede their application. Hence, a hybrid SBC-EMI-filter synthesis for a PES may enable operation using these fast-transition devices at high dv/dt and at higher power.

APPENDIX I

Some of the common nomenclature used is delineated as follows:

$T_{\rm kw}, T_{{\rm kw}_s}$	Different time horizons of the kth switching sequence ($k \in N$).
$\alpha_{\rm kn}$	Time allocation of the nth switching state in $k$thswitching sequence ($n \in N$).
n	A switching state in a switching sequence.
$A_{\rm kn}$, $B_{\rm kn}$	PES state matrices in continuous domain.
$x(t), \dot{x}(t)$	PES state and its derivative, PES dynamics.
$e(t)$	Error vector showing the deviation of PES states from steady-state values
A_{knd}, B_{knd}.$\hat{A}_{knd}$, $\widehat{B}_{knd}$	PES state matrices in discrete domain, and the online prediction model.
h, h_1	Total number of switching states in kth switching sequence of two different switching sequences
i	A discrete sample of the PES state.
$V_k(j), \nabla V_k(e)$	A piecewise-discrete (multiple) Lyapunov function for $k$thswitching sequence and its gradient
$P_{kn}.P$	A matrix whose positive definiteness must be checked and matrix that provides scaling of the terms in the generalized cost function.
$C(\alpha_{\rm kn}, T_{\rm kw})$	Generalized cost-function for PES control synthesis.
$\hat{x}^*$	PES steady state target values in PES cost-function.
$\alpha_{kn_{opt}}, T_{{\rm kw}_{opt}}$	The optimal values of $\alpha_{\rm kn}$ and $T_{\rm kw}$ that are fed to the PES power stage.
$\overline{\hat{A}_{knd}}, \overline{\hat{B}_{knd}}$	PES observer matrices in discrete domain.
Δ	Δ is designed to reduce the PES model-hardware inaccuracies in the closed-loop state observer.
$L_1,\ L_2, L_m$	Primary, secondary, and magnetizing inductance values of the Ćuk–PES.
$C_1, C_2,\ C_{\rm out}, C_d.R_d$	Primary, secondary, output, and damper capacitance/resistance (referred to primary side and across C_1) of the Ćuk–PES.
$IL_{\rm ref}$	Input inductor current reference of Ćuk–PES.
$V_{\rm ref}$	Output voltage reference for Ćuk–PES.
$iL_1(j)$	Predicted inductor current sample by the Ćuk–PES observer.
$V_{\rm out}(j)$	Output sensed voltage sample by PES sensor
δ_1,$G_p, G_I, \gamma_1, \gamma_2$	The weight-tuning factors in cost-function of the Ćuk–PES.
$\partial_1, \partial_2, \partial_3$	Parameters that does SBC in Modes 1 and 2
$\Delta iL_1(t).\Delta iL_{1_{\rm new}}(t)$	High-frequency ripple component of the input DM inductor current before and after EMI mitigation.
$iL_{\rm avg}$	Average component of the input inductor current.
n_1	Number of a generalized harmonic in Fourier series for CM/DM EMI prediction.
$C_{\rm dm}, C_{cm}$	Amplitude of a generalized harmonic in Fourier series for DM/CM EMI prediction
$C_{dm_{\rm new}}.C_{cm_{\rm new}}$	Amplitude of a generalized harmonic in Fourier series for DM/CM prediction after EMI mitigating sequence is applied
$i_{CM_{\rm total}}(t).i_{CM_{\rm total_{new}}}(t)$	Input CM current before and after EMI mitigation.
$C_{{\rm EMI}_{\rm dm/cm}}$	EMI standards for DM/CM EMI.

$V_{s_1}, V_{s_2}, V_{T_p}, V_{T_s}$	Primary and secondary GaN–FET device drain to source voltages and transformer primary and secondary voltage.
N_p, N_s	Transformer primary and secondary turns.
$C_{s_1}, C_{s_2}, C_{s_T}.i_{s_1}, i_{s_2}, i_{s_T}$	CM capacitances and currents (Fig. 8).
t_r, t_f	Generalized rise and fall time of a CM dv/dt node.
$v_m(w_m t)$	The nature of variation of $T_{\rm kw} \in \{T_{\rm kw_1}, \ldots T_{\rm kw_s}, \ldots, T_{\rm kw_{h_1}}\}$ in real-time to reduce EMI
$C_{\rm LISN1,2}, R_{\rm LISN1,2}, L_{\rm LISN1,2}$	LISN parameters.

APPENDIX II

For a generalized PES supplying a passive load, the PES dynamics for the nth switching state in the kth SS can be expressed in the form

$$\dot{x}\ (t) = A_{\rm kn} x\,(t) + B_{\rm kn}. \tag{A1}$$

Next, (A1) is translated to error coordinates using $e(t) = x(t) - x^*$, where $e(t)$ represents the error vector, while x^* represents the steady-state values of the PES states. In the error coordinate, (1) is modified as follows:

$$\dot{e}\,(t)\ = A_{\rm kn} e\,(t) + \overline{B_{\rm kn}} \tag{A2}$$

where $\overline{B_{\rm kn}} = -(B_{\rm kn} + A_{\rm kn} x^*)$. Discretizing (2), one obtains the following expression for jth discrete sample, (considering that the kth SS has total of h switching states):

$$e\,(i+1)\ = A_{knd} e\,(i) + B_{knd} \tag{A3}$$

where

$$A_{knd} = \prod_{n=1}^{2h} \exp^{A_{\rm kn} T_{\rm kw} \alpha_{k(2h-n+1)}} \tag{A4a}$$

$$\begin{aligned} B_{knd} = {} & \left[\left(\prod_{n\neq 1}^{2h} \exp^{A_{k(2h-n+1)} T_{\rm kw} \alpha_{k(i)}} \right) \right. \\ & \times \left(\exp^{A_{k1} T_{\rm kw} \alpha_{k1}} - I\right) A_{k1}^{-1} \overline{B_{k1}} \\ & + \left(\prod_{n\neq 12}^{2h} \exp^{A_{k(2h-n+1)} T_{\rm kw} \alpha_{k(i)}} \right) \left(\exp^{A_{k2} T_{\rm kw} \alpha_{k2}} - I\right) \\ & A_{k2}{}^{-} \overline{B_{k2}} + \cdots + (\exp^{A_{k2h} T_{\rm kw} \alpha_{k2h}} - I) A_{k2h}{}^{-1} \overline{B_{k2h}}. \end{aligned} \tag{A4b}$$

For the kth SS illustrated in Fig. 3(a), with h switching states satisfying $0 \le \alpha_{\rm kn} \le 1$, $\sum_{n=1}^{h} \alpha_{\rm kn} = 1$, and $P_{\rm kn} = P_{\rm kn}^T$ being positive-definite matrices, a piecewise-discrete (multiple) Lyapunov function $V_k(j) = \sum_{n=1}^{h} e(j)^T P_{\rm kn} e(j)$ is used to obtain the gradient of the multiple Lyapunov function:

$$\begin{aligned} \nabla V_k\ (e) &= V_k\ (i+1) - V_k\,(i) \\ &= \sum_{n=1}^{h} \alpha_{\rm kn} \left(e(i+1)^T P_{\rm kn} e\,(i+1) - e(i)^T P_{\rm kn} e\,(i) \right). \end{aligned} \tag{A5}$$

According to Lyapunov method of stability analysis for a discrete system, the PES state trajectories converge to (i.e., reach) an orbit if $\nabla V_k(e) < 0$ which results in the following linear matrix inequality (LMI) for any generalized PES:

$$\sum_{n=1}^{h} \alpha_{\rm kn} \begin{bmatrix} (A_{knd}^T P_{kn} A_{knd} - P_{\rm kn}) & A_{knd}^T P_{kn} B_{knd} \\ B_{knd}^T P_{kn} A_{knd} & B_{knd}^T P_{kn} B_{knd} \end{bmatrix} < 0 \tag{A6}$$

which is formulated as a feasibility problem and solved using the LMI tool in MATLAB. Hence, depending on the PES topology and its switching behavior along with the knowledge of the specific load, once a reachability set of $\alpha_{\rm kn}$ and $T_{\rm kw}$ is obtained from the extensive offline analysis, they can be used to solve the SBC online optimal control problem. The detailed derivation of (A6) is delineated in [30].

APPENDIX III

The matrices $\hat{A}_{\rm kn}$ and $\hat{B}_{\rm kn}$ for the two switching states of the Ćuk–PES, expressed as $\hat{A}_{kn1}$ and $\hat{B}_{kn1}$ and $\hat{A}_{kn2}$ and $\hat{B}_{kn2}$, respectively, are defined as follows, where the symbols of the passive components are defined in Fig. 7. R_d and C_d are the RC branch parameters in parallel to the blocking capacitor, referred to the primary side of the HFT:

$$\hat{A}_{kn1} = \begin{bmatrix} 0 & 0 & 0 & 0 & 0 & 0 & 0 \\ 0 & 0 & 0 & \frac{2}{L_2} & \frac{1}{L_2} & \frac{-1}{L_2} & 0 \\ 0 & 0 & 0 & \frac{-1}{L_m} & 0 & 0 & 0 \\ 0 & \frac{-2}{C_1} & \frac{1}{C_1} & \frac{-1}{R_d C_1} & 0 & 0 & \frac{1}{R_d C_1} \\ 0 & \frac{-1}{C_2} & 0 & 0 & 0 & 0 & 0 \\ 0 & \frac{1}{C_{out}} & 0 & 0 & 0 & \frac{-1}{R_3 C_{out}} & 0 \\ 0 & 0 & 0 & \frac{1}{R_d C_d} & 0 & 0 & \frac{-1}{R_d C_d} \end{bmatrix}$$

$$\hat{B}_{kn1} = \begin{bmatrix} \frac{V_{in}}{L_1} \\ 0 \\ 0 \\ 0 \\ 0 \\ 0 \\ 0 \end{bmatrix}$$

$$\hat{A}_{kn2} = \begin{bmatrix} 0 & 0 & 0 & \frac{-1}{L_1} & \frac{-1}{2L_1} & 0 & 0 \\ 0 & 0 & 0 & 0 & 0 & \frac{-1}{L_2} & 0 \\ 0 & 0 & 0 & 0 & \frac{1}{2L_m} & 0 & 0 \\ 0 & \frac{1}{C_1} & 0 & \frac{-1}{R_d C_1} & 0 & 0 & \frac{1}{R_d C_1} \\ \frac{1}{2C_2} & 0 & \frac{-1}{2C_2} & 0 & 0 & 0 & 0 \\ 0 & \frac{1}{C_{out}} & 0 & 0 & 0 & \frac{-1}{R_3 C_{out}} & 0 \\ 0 & 0 & 0 & \frac{1}{R_d C_d} & 0 & 0 & 0 \end{bmatrix}$$

$$\hat{B}_{kn1} = \begin{bmatrix} \frac{V_{in}}{L_1} \\ 0 \\ 0 \\ 0 \\ 0 \\ 0 \\ 0 \end{bmatrix}$$

The reduced-order PES matrices $\hat{A}_{knd}$, $\hat{B}_{knd}$, $\overline{\hat{A}_{knd}}$, and $\overline{\hat{B}_{knd}}$ can be expressed as follows:

$$\hat{A}_{knd} = \prod_{n=1}^{2h} \exp^{\hat{A}_{\rm kn} T_{\rm kw} \alpha_{k(2h-n+1)}} \tag{A7}$$

$$\begin{aligned}\hat{B}_{knd} = [&\left(\prod_{n\neq 1}^{2h} \exp^{\hat{A}_{k(2h-n+1)} T_{\rm kw} \alpha_{k(n)}}\right) \\ &\times \left(\exp^{\hat{A}_{k1} T_{\rm kw} \alpha_{k1}} - I\right) \hat{A}_{k1}^{-1} \hat{B}_{k1} \\ &\left(\prod_{n\neq 12}^{2h} \exp^{\hat{A}_{k(2h-n+1)} T_{\rm kw} \alpha_{k(n)}}\right) \left(\exp^{\hat{A}_{k2} T_{\rm kw} \alpha_{k2}} - I\right) \hat{A}_{k2}^{-1} \hat{B}_{k2} \\ &+ \cdots\cdots + \left(\exp^{\hat{A}_{k2h} T_{\rm kw} \alpha_{k2h}} - I\right) \hat{A}_{k2h}^{-1} \hat{B}_{k2h}\end{aligned} \tag{A8}$$

$$\overline{\hat{A}_{knd}} = \prod_{n=1}^{2h} \exp^{\hat{A}_{\rm kn} T_{\rm kw} (\alpha_{k(2h-n+1)} + \Delta(\alpha_{k(2h-n+1)}))}$$

$$\begin{aligned}\overline{\hat{B}_{knd}} = [&\left(\prod_{n\neq 1}^{2h} \exp^{\hat{A}_{k(2h-n+1)} T_{\rm kw} (\alpha_{k(n)} + \Delta\alpha_{k(n)})}\right) \\ &\left(\exp^{\hat{A}_{k1} T_{\rm kw} (\alpha_{k1} + \Delta\alpha_{k1})} - I\right) \hat{A}_{k1}^{-1} \hat{B}_{k1} \\ &\left(\prod_{n\neq 12}^{2h} \exp^{\hat{A}_{k(2h-n+1)} T_{\rm kw} (\alpha_{k(n)} + \Delta\alpha_{k(n)})}\right) \\ &\left(\exp^{\hat{A}_{k2} T_{\rm kw} (\alpha_{k2} + \Delta\alpha_{k2})} - I\right) \hat{A}_{k2}^{-1} \hat{B}_{k2} \\ &+ \left(\exp^{\hat{A}_{k2h} T_{\rm kw} (\alpha_{k2h} + \Delta\alpha_{k2h})} - I\right) \hat{A}_{k2h}^{-1} \hat{B}_{k2h}.\end{aligned} \tag{A9}$$

The correction terms, denoted by Δ, are designed to reduce the PES model-hardware inaccuracies, and have been described in [30].

Appendix IV

For a dc/dc PES operating in steady state with a time horizon $T_{\rm kw_s}$, any PES state [say $\hat{x}_1(t)$] can be generalized as a periodic series in time domain like

$$\hat{x}_1(t) = \sum_{n_1=0}^{\infty} C_{n_1} exp^{\left(2\pi j \left(n_1 T_{\rm kw_s}^{-1}\right) t\right)} \tag{A10}$$

where C_{n_1} is the magnitude of the n_1th harmonic of the time horizon $T_{\rm kw_s}$. Now, instead of a fixed time horizon $T_{\rm kw_s}$, we consider a new time horizon $T_{\rm kw}$. As defined in Fig. 5, $T_{\rm kw}$ is formed of discrete time horizons $T_{\rm kw_i}^{-1} = T_{\rm kw_s}^{-1} + \Delta T_{\rm kw}^{-1} v_m(w_m t)$. $T_{\rm kw_i}^{-1}$ starts at $T_{\rm kw_s}^{-1}$ for $i = 1$, reaches $T_{\rm kw_i}^{-1} = T_{\rm kw_s}^{-1} + \Delta T_{\rm kw}^{-1}$ at $i = h_1/2$, and ends again at $T_{\rm kw_i}^{-1} = T_{\rm kw_s}^{-1}$ for $i = h_1$ as defined in Fig. 5. If $v_m(w_m t) = \sin(w_m t)$, the PES state $\hat{x}_1(t)$ with the new horizon $T_{\rm kw}$ can again be written as a periodic series in time domain as

$$\hat{x}_{1_{\rm new}}(t) = \sum_{n_1=0}^{\infty} C_{n_1} \exp^{\left(2\pi j \left(n_1 T_{\rm kw_s}^{-1}\right) t + n_1 \int_0^t (v_m(\tau)(d\tau))(\Delta T_{\rm kw})^{-1}\right)} \tag{A11}$$

where

$$\Delta T_{\rm kw}^{-1} = T_{\rm kw_{h_{1/4}}}^{-1} - T_{\rm kw_s}^{-1}. \tag{A12}$$

Using mathematical manipulations formulated in [37] and [14], (A11) can be simplified to the form given by

$$\hat{x}_1(t) = \sum_{n_1=0}^{\infty} \sum_{m_1=-\infty}^{\infty} C_{n_{1new}} \exp^{\left(2\pi j \left(n_1 T_{\rm kw_s}^{-1} + m_1 T_{\rm kw}^{-1}\right) t\right)} \tag{A13}$$

where

$$C_{n_{1_{\rm new}}} = C_{m_1 n_1} \tag{A14a}$$

$$T_{\rm kw} = \left(\frac{2\pi}{w_m}\right)^{-1} \tag{A14b}$$

$$C_{m_1} = j^{-1} J_{m_1}\left(n_1 \Delta T_{\rm kw}^{-1} T_{\rm kw}\right) \tag{A14c}$$

$$C_{m_1 n_1} = C_{n_1} C_{m_1} \exp\left(j n_1 \Delta T_{\rm kw}^{-1} T_{\rm kw}\right) \tag{A14d}$$

and J_{m_1} is the Jacobian function [37].

Acknowledgment

The authors would like to thank Ankit Gupta (former doctoral student) and Moein Mohamadi (current doctoral student), members in the Laboratory for Energy and Switching-Electronic Systems at the University of Illinois at Chicago, for their invaluable suggestions in the PCB design of the GaN-based Ćuk PES and magnetic design of the common mode inductor.

References

[1] A. Kulkarni, A. Gupta, and S. K. Mazumder, "Resolving practical design issues in a single-phase grid-connected GaN-FET-based differential-mode inverter," *IEEE Trans. Power Electron.*, vol. 33, no. 5, pp. 3734–3751, May 2018.

[2] "GN001 application guide design with GaN enhancement mode HEMT," GaN Systems Inc., Ottawa, ON, Canada, 2018.

[3] T. Hegarty, "An overview of conducted EMI specifications for power supplies," Texas Instruments Whitepaper, Feb. 2, 2018.

[4] K. Raggl, S. Member, T. Nussbaumer, J. W. Kolar, and S. Member, "Guideline for a simplified differential-mode EMI filter design," *IEEE Trans. Ind. Electron.*, vol. 57, no. 3, pp. 1031–1040, Apr. 2010.

[5] A. Nagel and R. W. De Doncker, "Systematic design of EMI-filters for power converters," in *Proc. Conf. Rec. IEEE Ind. Appl. Conf. 35th IAS Annu. Meeting World Conf. Ind. Appl. Elect. Energy*, 2000, pp. 2523–2525.

[6] L. Xing, J. Sun, and S. Member, "Optimal damping of multistage EMI filters," *IEEE Trans. Power Electron.*, vol. 27, no. 3, pp. 1220–1227, Mar. 2012.

[7] Z. Hao, "Simple solution for input filter stability issue in dc/dc converters," Application report, Texas Instruments, Dallas, TX, USA, Apr. 2019.

[8] G. Spiazzi and J. A. Pomilio, "Interaction between EMI filter and power factor preregulators with average current control: Analysis and design considerations," *IEEE Trans. Ind. Electron.*, vol. 46, no. 3, pp. 577–584, Jun. 1999.

[9] L. Xing, "Optimal damping of EMI filter input impedance" *IEEE Trans. Ind. Appl.*, vol. 47, no. 3, pp. 1432–1440, May/Jun. 2011.

[10] L. Yang *et al.*, "Modeling and characterization of a 1KW CCM PFC converter for conducted EMI prediction," in *Proc. 19th Annu. IEEE Appl. Power Electron. Conf. Expo.*, 2004, pp. 763–769.

[11] K. Mainali and R. Oruganti, "Simple analytical models to predict conducted EMI noise in a power electronic converter," in *Proc. 33rd Annu. Conf. IEEE Ind. Electron. Soc.*, 2007, pp. 1930–1936.

[12] S. Walder, X. Yuan, I. Laird, and J. J. O. Dalton, "Identification of the temporal source of frequency domain characteristics of SiC MOSFET based power converter waveforms," in *Proc. IEEE Energy Convers. Congr. Expo.*, 2016, pp. 1–8.

[13] P. Kong, Y. Jiang, and F. C. Lee, "Common mode EMI noise characteristics of low-power ac-dc converters," *IEEE Trans. Power Electron.*, vol. 27, no. 2, pp. 731–738, Feb. 2012.
[14] B. van der Pol, "The fundamental principles of frequency modulation," *J. Inst. Elect. Eng. - Part III Radio Commun. Eng.*, vol. 93, no. 23, pp. 153–158, May 1946.
[15] J. Balcells, A. Santolaria, A. Orlandi, D. González, and J. Gago, "EMI reduction in switched power converters using frequency modulation techniques," *IEEE Trans. Electromagn. Compat.*, vol. 47, no. 3, pp. 569–576, Aug. 2005.
[16] J. A. S. Lorenzo, "SSCG methods of EMI emissions reduction applied to switching power converters," in *Proc. IEEE 35th Annu. Electron. Specialists Conf.*, 2004, pp. 292–296.
[17] A. Santolaria, J. Balcells, and D. Gonzalez, "Theoretical & experimental results of power converter frequency modulation," in *Proc. IEEE 28th Annu. Conf. Ind. Electron. Soc.*, 2002, pp. 193–197.
[18] F. Lin and D. Y. Chen, "Reduction of power supply EMI emission by switching frequency modulation," *IEEE Trans. Power Electron.*, vol. 9, no. 1, pp. 132–137, Jan. 1994.
[19] A. Santolaria, "Effects of switching frequency modulation on the power converter's output voltage," *IEEE Trans. Ind. Electron.*, vol. 56, no. 7, pp. 2729–2737, Jul. 2009.
[20] D. Stepins, "Effect of frequency modulation on input current of switch-mode power converter," in *Proc. 39th Annu. Conf. IEEE Ind. Electron. Soc.*, 2013, pp. 683–688.
[21] T. Geyer, "Computationally efficient model predictive direct torque control," *IEEE Trans. Power Electron.*, vol. 26, no. 10, pp. 2804–2816, Oct. 2011.
[22] P. Karamanakos, T. Geyer, and S. Manias, "Direct model predictive current control strategy of dc-dc boost converters," *IEEE J. Emerg. Sel. Topics Power Electron.*, vol. 1, no. 4, pp. 337–346, Dec. 2013.
[23] T. Geyer, "A comparison of control and modulation schemes for medium-voltage drives: Emerging predictive control concepts versus PWM-based schemes," *IEEE Trans. Ind. Appl.*, vol. 47, no. 3, pp. 1380–1389, May 2011.
[24] S. Vazquez, A. Marquez, R. Aguilera, D. Quevedo, J. I. Leon, and L. G. Franquelo, "Predictive optimal switching sequence direct power control for grid-connected power converters," *IEEE Trans. Ind. Electron.*, vol. 62, no. 4, pp. 2010–2020, Apr. 2015.
[25] S. Vazquez *et al.*, "Model predictive control: A review of its applications in power electronics," *IEEE Ind. Electron. Mag.*, vol. 8, no. 1, pp. 16–31, Mar. 2014.
[26] J. Neely, R. DeCa, and S. Pekarek, "Real-time model predictive control of the Ćuk converter," in *Proc. IEEE 12th Workshop Control Model. Power Electron.*, 2010, pp. 1–8.
[27] R. Vargas, U. Ammann, and J. Rodríguez, "Predictive approach to increase efficiency and reduce switching losses on matrix converters," *IEEE Trans. Power Electron.*, vol. 24, no. 4, pp. 894–902, Apr. 2009.
[28] A. F. Limon, I. Alvarado, and T. Alamo, "Nonlinear MPC for tracking piece-wise constant reference signals," *IEEE Trans. Autom. Control*, vol. 63, no. 11, pp. 3735–3750, Nov. 2018.
[29] A. Tajfar and S. K. Mazumder, "Sequence-based control of an isolated dc/ac matrix converter," *IEEE Trans. Power Electron.*, vol. 31, no. 2, pp. 1757–1773, Feb. 2016.
[30] D. Chatterjee and S. K. Mazumder, "Switching-sequence control of a higher-order power-electronic system driving a pulsating load," *IEEE Trans. Power Electron.*, vol. 35, no. 1, pp. 1096–1110, Jan. 2020.
[31] S. K. Mazumder and K. Acharya, "Multiple lyapunov function based reaching condition for orbital existence of switching power converters," *IEEE Trans. Power Electron.*, vol. 23, no. 3, pp. 1449–1471, May 2008.
[32] Z. Chen, "PI and sliding mode control of a cuk converter," *IEEE Trans. Power Electron.*, vol. 27, no. 8, pp. 3695–3703, Aug. 2012.
[33] R. Redl and N. O. Sokal, "Near-optimum dynamic regulation of dc-dc converters using feed-forward of output current and input voltage with current-mode control," *IEEE Trans. Power Electron.*, vol. PE-1, no. 3, pp. 181–192, Jul. 1986.
[34] P. Cortes *et al.*, "Guidelines for weighting factors design in model predictive control of power converters and drives," in *Proc. IEEE Int. Conf. Ind. Technol.*, 2009, pp. 1–7.
[35] Q. Ji, X. Ruan, and Z. Ye, "The worst conducted EMI spectrum of critical conduction mode boost PFC converter," *IEEE Trans. Power Electron.*, vol. 30, no. 3, pp. 1230–1241, Mar. 2015.
[36] K. Fu, W. Chen, and S. Lin, "A general transformer evaluation method for common-mode noise behavior," *Energies*, vol. 12, no. 10, 2019, Art. no. 1984.
[37] J. Huang and R. Xiong, "Study on modulating carrier frequency twice in SPWM single-phase inverter," *IEEE Trans. Power Electron.*, vol. 29, no. 7, pp. 3384–3392, Jul. 2014.

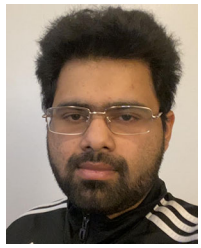

Debanjan Chatterjee (Student Member, IEEE) received the B.E. degree in electrical engineering from Jadavpur University, Kolkata, India, in 2015. He is currently working toward the Ph.D. degree in electrical and computer engineering with the University of Illinois at Chicago, Chicago, IL, USA.

His research interests include digital control and modulation of power electronic converters, and model predictive, switching sequence, and switching transition controllers for GaN-based power electronic systems.

Sudip K. Mazumder (Fellow, IEEE) received the M.S. degree in electrical power engineering from Rensselaer Polytechnic Institute, Troy, NY, USA, in 1993, and the Ph.D. degree in electrical and computer engineering from Virginia Tech, Blacksburg, VA, USA, in 2001.

He has been a Professor with the University of Illinois, Chicago, IL, USA, since 2001, and the President with Next Watt LLC, since 2008. He has around 30 years of professional experience and has held R&D and design positions in leading industrial organizations, and has also served as a Technical Consultant for several industries. He has developed novel multiscale methodologies for controlling power-electronic systems and networks at wide-/narrow-bandgap semiconductor device level resulting in plurality of practical applications. His research interests include high-frequency-link power electronics including hybrid modulation and differential-mode-converter topology and optically controlled power semiconductor devices and power electronics.

Prof. Mazumder was a Distinguished Lecturer for the IEEE PELS between 2016 and 2019. He was named a Fellow of the American Association for the Advancement of Science in 2020 for distinguished contributions to the field of multiscale control and analysis of power-electronic systems and a Fellow of the Institute of Electrical and Electronics Engineers in 2016 for his contributions to the analysis and control of power-electronic systems. Currently, he serves as the Editor-in-Chief at Large for the IEEE TRANSACTIONS OF POWER ELECTRONICS (TPEL). He has been serving as an Administrative Committee Member and as a Member-at-Large for IEEE PELS since 2015 and 2020, respectively. He also served as the Chair for the IEEE PELS Technical Committee on Sustainable Energy Systems from 2015 to 2020. At UIC, he is the recipient of the Distinguished Researcher Award in Natural Sciences and Engineering (2020), the Inventor of the Year Award (2014), and the University Scholar (2013). He was also the recipient of the several IEEE awards including Prize Paper Award from the IEEE TPEL and the IEEE International Future Energy Challenge Award, the U.S. Office of Naval Research Young Investigator Award (2005), and the U.S. National Science Foundation CAREER Award (2003).